

MS Thesis in Physics

**Synthesis and Physical Characterization  
of Pyrochlore oxides**

**Haritha S Rajeev**  
BS-MS Dual degree student

Under the guidance of  
**Dr. Surjeet Singh**

Thesis submitted towards the partial fulfilment of  
BS MS Dual degree program




Indian Institute of Science Education and Research, Pune

# CERTIFICATE



This is to certify that this dissertation entitled **Synthesis and Physical Characterization of Pyrochlore oxides** towards the partial fulfilment of the BS-MS dual degree programme at the Indian Institute of Science Education and Research, Pune represents the work carried out by **Haritha S Rajeev** at **IISER Pune** under the supervision of **Dr. Surjeet Singh** during the academic year 2018-2019.

  
Haritha S Rajeev

  
Dr. Surjeet Singh

# DECLARATION

I hereby declare that the matter embodied in the report entitled **Synthesis and Physical Characterization of Pyrochlore oxides** are the results of the work carried out by me at the Department of Physics, IISER Pune, under the supervision of Dr. Surjeet Singh and the same has not been submitted elsewhere for any other degree.



Haritha S Rajeev



Dr. Surjeet Singh

## ACKNOWLEDGEMENT

I here express my great sense of gratitude to Dr. Surjeet Singh for providing me the opportunity to work in his lab for my MS thesis. I acknowledge his valuable suggestions and reviews which were immensely helpful to carry out my project.

I also express my sincere gratitude to Prachi Telang for her most valuable guidance and support which activated my thought culminating in this project. Under her guidance I learnt about different methods to prepare samples, study their properties and analyse the results during the course of work.

I would like to acknowledge the services of Mr. Nilesh, Mr. Yathish and Mr. Anil for their technical support.

I also wish to thank Dr. Luminita Harnagea, Dibyatha, Sourabh, Navita, Rabrindranath Bag, Sancheyta, Prakash, Anupam, Nupur and Pragna for their cooperation, support and illuminating discussions.

I acknowledge gratefully IISER Pune, for providing me a platform to nurture my scientific career with its high end research facilities.

# Abstract

5d Transition metal oxides with  $\text{Ir}^{4+}$  as the transition metal ion has been of great interest due to its comparable on site coulomb interaction and spin orbit coupling, which together result in a rich array of physical properties. The iridates of the pyrochlore structure are a promising candidate for realizing the Weyl semimetals. They change their physical properties from that of an antiferromagnetic insulator for smaller or heavier rare earths (i.e.,  $A = \text{Gd, Tb, Dy, Ho, Er, and Yb}$ , including  $\text{Y}$ ) to an exotic, nonmagnetic metal for  $\text{Pr}_2\text{Ir}_2\text{O}_7$ . The intermediate members corresponding to  $A = \text{Nd, Sm, and Eu}$  show a thermally induced metal-insulator transition. Literature reveals that stuffing in  $\text{Eu}_2\text{Ir}_2\text{O}_7$  show a strong correlation between the physical properties and structure. This project started with the idea of understanding the effect of stoichiometry on the physical properties of  $\text{Sm}_2\text{Ir}_2\text{O}_7$ , which is lacking for the pyrochlore iridates. Till now, all the pyrochlore iridate sample reported in the literature are synthesized using the conventional ceramic route, which takes more than 600 hrs of sintering to stabilize the pyrochlore phase along with significant  $\text{IrO}_2$  losses. Through this project 6 samples of lanthanide pyrochlore iridates ( $\text{Ln} = \text{Pr, Sm, Gd, Er and Yb}$ ) were synthesized using a wet-chemical technique through a single sintering. The wet-chemical method is shown to be an efficient way of obtaining single-phase pyrochlore iridate samples with sintering duration as low as 12 hrs and negligible  $\text{IrO}_2$  losses. As the final stoichiometry can affect the physical properties, comparison of results obtained from the solid-state reaction technique and the wet-chemical route were done. The resistivity data suggest that none of the wet-chemically synthesized samples exhibit the  $\frac{1}{T^\alpha}$ , (with  $\alpha = 1$  or  $4$ ) expected from weyl semimetallic nature of the electronic structure. phase. A metal to insulator transition was seen for  $\text{Sm}_2\text{Ir}_2\text{O}_7$  and  $\text{Gd}_2\text{Ir}_2\text{O}_7$  concomitant with AFM ordering in the insulating regime. The specific heat data were analyzed, using an equation considering schottky anomaly, electronic and phonon contributions.

# Contents

<b>1</b>	<b>Introduction</b>	<b>8</b>
<b>2</b>	<b>Pyrochlore structure</b>	<b>11</b>
<b>3</b>	<b>Pyrochlore iridates</b>	<b>13</b>
<b>4</b>	<b>Experimental techniques</b>	<b>16</b>
4.1	X-ray diffraction . . . . .	16
4.2	Scanning electron microscopy . . . . .	17
4.3	Physical Property Measurement System . . . . .	17
4.3.1	Transport property measurements . . . . .	18
4.3.2	Magnetic property measurements . . . . .	19
4.3.3	Heat Capacity measurements . . . . .	19
<b>5</b>	<b>Sm<sub>2±x</sub>Ir<sub>2∓x</sub>O<sub>7</sub>, x=1, 0.04, 0.02 bulk material</b>	<b>20</b>
5.1	Synthesis of samples . . . . .	20
5.2	Structural characterization of samples . . . . .	21
5.3	Summary and Conclusions . . . . .	23
<b>6</b>	<b>A<sub>2</sub>Ir<sub>2</sub>O<sub>7</sub>, A= Pr, Gd, Sm, Dy, Er, Yb</b>	<b>24</b>
6.1	Wet chemical synthesis route for Pyrochlore iridates . . . . .	24
6.1.1	Synthesis of bulk samples . . . . .	25

6.1.2	Structural characterization of the samples . . . . .	25
6.1.3	Structural comparison of the samples synthesized via solid and wet chemical route . . . . .	28
6.1.4	Summary and conclusion . . . . .	30
6.2	Physical Property Measurements . . . . .	30
6.2.1	Electrical transport measurements . . . . .	30
6.2.2	Magnetic measurements . . . . .	36
6.2.3	Heat capacity measurements . . . . .	37
6.2.4	Summary and conclusions . . . . .	40
6.3	Outlook . . . . .	40

# List of Figures

2.1	Pyrochlore structure . . . . .	12
3.1	A schematic phase diagram showing various ground states depending on the strength of spin orbit coupling (SOC) $\lambda$ and Coulomb repulsion $U$ [1]	13
3.2	(a) dirac node, (b) pair of weyl nodes . . . . .	14
3.3	(a)(b)(c) Energy level splitting of 5d orbitals under octahedral field symmetry and spin orbit coupling, (b)All in all out ground state in $\text{Ir}^{4+}$ . . .	15
3.4	(a) Phase diagram and (b) electrical resistivities of $\text{A}_2\text{Ir}_2\text{O}_7$ ( $A = \text{Pr, Nd, Sm, Eu, Gd, Tb, Dy, Ho, Y}$ ) . . . . .	15
4.1	Image of the resistivity contacts made for measurement in PPMS . . . . .	18
5.1	X Ray diffraction pattern for $\text{Sm}_{2\pm x}\text{Ir}_{2\mp x}\text{O}_7$ , ( $x= 0, 0.02, 0.04$ ) . . . . .	21
5.2	Simulated and observed X Ray diffraction pattern for $\text{Sm}_{2.04}\text{Ir}_{1.96}\text{O}_7$ . . .	22
6.1	Wet chemical synthesis route for $\text{A}_2\text{Ir}_2\text{O}_7$ , $A=\text{Pr, Sm, Gd, Dy, Er, Yb}$ .	25
6.2	X Ray diffraction pattern, [222] Peak shift and lattice parameter variation for $\text{A}_2\text{Ir}_2\text{O}_7$ , $A=\text{Pr, Sm, Gd, Dy, Er, Yb}$ . . . . .	26
6.3	SEM images for $\text{Ln}_2\text{Ir}_2\text{O}_7$ , $\text{Ln}=\text{Pr, Sm, Gd, Dy, Er, Yb}$ . . . . .	27
6.4	X ray diffraction pattern comparison for ) $\text{Sm}_2\text{Ir}_2\text{O}_7$ synthesized via solid state reaction and wet chemical reaction methods . . . . .	28
6.5	Microstructure comparison for $\text{Sm}_2\text{Ir}_2\text{O}_7$ synthesized via solid state reaction and wet chemical reaction methods using SEM images . . . . .	29
6.6	(a) $\rho(T)/\rho(300 \text{ K})$ for $\text{A}_2\text{Ir}_2\text{O}_7$ , with $A=\text{Pr, Sm, Gd, Dy, Er, Yb}$ ), (b) $\rho(T)/\rho(300 \text{ K})$ versus $\ln(T)$ plot for $\text{Pr}_2\text{Ir}_2\text{O}_7$ in the temperature range 2K to 100K .	30



6.7	$\rho(T)/\rho(300\text{ K})$ for $\text{Sm}_2\text{Ir}_2\text{O}_7$ , synthesized via solid state reaction and wet chemical method (WC). In the figure two samples each of $\text{Sm}_2\text{Ir}_2\text{O}_7$ , for each synthesis method is shown. Wet chemical method was repeated for the sample to check the reproducibility. Resistivity data for the two samples of the same compound synthesized at two different times via solid state method, to compare its low temperature magnitude with that of wet chemical method . . . . .	31
6.8	Resistivity versus temperature of $\text{Pr}_2\text{Ir}_2\text{O}_7$ . The open black circles are the observed resistivity point. The solid red, blue, green and violet lines are best fits of the resistivity for arrhenius behavior, variable range hopping with electronic correlations, variable range hopping and power law. . . . .	33
6.9	Resistivity versus temperature of $\text{Sm}_2\text{Ir}_2\text{O}_7$ . The open black circles are the observed resistivity point. The solid red, blue, green and violet lines are best fits of the resistivity for arrhenius behavior, variable range hopping with electronic correlations, variable range hopping and power law. . . . .	33
6.10	Resistivity versus temperature of $\text{Gd}_2\text{Ir}_2\text{O}_7$ . The open black circles are the observed resistivity point. The solid red, blue, green and violet lines are best fits of the resistivity for arrhenius behavior, variable range hopping with electronic correlations, variable range hopping and power law. . . . .	34
6.11	Resistivity versus temperature of $\text{Dy}_2\text{Ir}_2\text{O}_7$ . The open black circles are the observed resistivity point. The solid red, blue, green and violet lines are best fits of the resistivity for arrhenius behavior, variable range hopping with electronic correlations, variable range hopping and power law. . . . .	34
6.12	Resistivity versus temperature of $\text{Er}_2\text{Ir}_2\text{O}_7$ . The open black circles are the observed resistivity point. The solid red, blue, green and violet lines are best fits of the resistivity for arrhenius behavior, variable range hopping with electronic correlations, variable range hopping and power law. . . . .	35
6.13	Resistivity versus temperature of $\text{Yb}_2\text{Ir}_2\text{O}_7$ . The open black circles are the observed resistivity point. The solid red, blue, green and violet lines are best fits of the resistivity for arrhenius behavior, variable range hopping with electronic correlations, variable range hopping and power law. . . . .	35
6.14	$\chi(T)$ versus $T$ $\text{A}_2\text{Ir}_2\text{O}_7$ , $\text{A}=\text{Sm}$ . . . . .	36
6.15	$1/\chi(T)$ versus $T$ $\text{A}_2\text{Ir}_2\text{O}_7$ , $\text{A}=\text{Sm}, \text{Gd}, \text{Dy}, \text{Er}, \text{Yb}$ . . . . .	37

6.16 Comparison of Specific heat ( $C_p$ ) for $\text{Sm}_2\text{Ir}_2\text{O}_7$ in the present study and literature [2] . . . . .	38
6.17 Specific heat data comparison between samples synthesized via solid state reaction and wet chemical method for $\text{Sm}_2\text{Ir}_2\text{O}_7$ . . . . .	39
6.18 Specific heat data comparison between samples synthesized via solid state reaction and wet chemical method for $\text{Sm}_2\text{Ir}_2\text{O}_7$ . . . . .	39

# Chapter 1

## Introduction

Transition metal oxides (TMOs) have long been studied mainly because they display a wide variety of unusual structural and magnetic properties including metal-insulator transition, high- $T_c$  super conductivity, exotic spin ordering, etc [3]. For a TMO there are several energy scales to be considered including the on-site Coloumb repulsion ( $U$ ), spin-orbit coupling ( $\lambda$ ), crystal field splitting ( $\Delta$ ) and the hopping term ( $t$ ). Significant theoretical as well as experimental studies have been carried out on 3d transition metal oxide, which have localized 3d states, yielding high  $U$  and small band width. Most of them are Mott insulators. If only  $U$  and band width are considered, the 4d and 5d TMOs, which have extended d orbitals, a less insulating ground state is expected. But anomalous insulating state have been reported for these materials which emphasizes the significance of considering correlation effects. At the same time spin-orbit coupling term  $\lambda$  which scales with the atomic number, and contributions comparable to  $U$ , is also of significance in 4d/5d transition metal oxides [4]. Small changes brought in to these system either by pressure, doping, temperature, electric field or magnetic field results in a rich behaviour. Recently 5d transition metal oxides with Ir as the 5d transition element has been of significant interest for theoretical modelling as well as experimental research, to understand the interplay of various interactions explained above.

The geometrically frustrated pyrochlore oxides ( $A_2B_2O_7$ ) are well-known to host exotic quantum many-body ground states, including quantum spin liquids and spin ices. Pyrochlore oxides crystallizes in a cubic symmetry with two non-equivalent oxygen sites, namely, 48f and 8b. In this structure the only variable parameters are the unit cell edge

length (a), and the x-coordinate of the oxygen ion at the 48f site (x, 0.125, 0.125). The structure consists of interpenetrating networks of corner shared tetrahedrons formed by A and B cations [5]. The spins in the lattice result in geometric frustration forming a degenerate manifold of ground states rather than a single stable ground state. Even slight perturbation can induce instabilities in such systems [2].

The Pyrochlore iridates change their physical properties from a completely non magnetic metal for larger rare earth ion (A=Pr) to that of an antiferromagnetic insulator for smaller rare earth ions (A = Gd, Tb, Dy, Ho, Er, and Yb, including Y). The intermediate members including Nd, Sm, and Eu show a thermally induced metal to insulator transition at  $T_{MI}$ . The onset of insulating behavior is concomitant with anti-ferromagnetic ordering of  $\text{Ir}^{4+}$  moments at  $T_N$  [6]. These intermediate members are proposed to stabilize a novel topological phase called the Weyl Semimetal [7].

The physical properties of pyrochlore iridates are highly correlated with the structure which can be tuned by pressure or doping. The slope of resistivity ( $\rho$ ) versus temperature plot  $\frac{d\rho}{dT}$  is expected to be positive above  $T_{MI}$  when the sample is in its metallic state and negative below  $T_{MI}$  in its insulating state. Recent pressure studies on  $\text{Eu}_2\text{Ir}_2\text{O}_7$  by Tafti et al, reveals a change in sign of  $\frac{d\rho}{dT}$  in metallic state from negative for low or ambient pressure to positive above 6 GPa [8]. Similarly, Liu et al, reported that in  $\text{Sm}_2\text{Ir}_2\text{O}_7$ , external pressure changes not only the slope of  $\rho$  versus T above  $T_{MI}$  but the value of  $T_{MI}$  itself decrease almost linearly with increasing pressure [9]. The stark sample dependence on the sign of slope above  $T_{MI}$  was later investigated by stuffing studies on  $\text{Eu}_2\text{Ir}_2\text{O}_7$ , the results of which indicated that due to  $\text{Eu}^{3+}$  and  $\text{Ir}^{4+}$  ionic size mismatch, a minor off-stoichiometry and the resulting changes in unit cell volume can lead to chemical pressure sufficient enough to cause anomalies above  $T_{MI}$  [7]. A systematic study of stuffing is lacking in  $\text{Sm}_2\text{Ir}_2\text{O}_7$  which is important to understand the effect of off-stoichiometry in explaining the sign of  $\frac{d\rho}{dT}$ . Synthesis of iridate pyrochlores is highly tricky due to the loss of  $\text{IrO}_2$ . As  $\text{IrO}_2$  tend to sublime at a temperature approximately above  $1000^\circ\text{C}$  due to its high vapor pressure as well as the formation of volatile  $\text{IrO}_3$ , the  $\text{IrO}_2$  loss can be quite significant if the sample is not sintered for sufficient time at lower temperatures for  $\text{A}_2\text{O}_3$  and  $\text{IrO}_2$  to react. In studies by Matsuhira et al polycrystalline samples of  $\text{A}_2\text{Ir}_2\text{O}_7$  (A = Pr, Nd, Sm, Eu, Gd, Tb, Dy, and Ho) underwent sintering for a duration of 336 hrs with several intermittent grindings above  $1200^\circ\text{C}$  [2]. Telang et al studies

report a sintering duration of 374 h with 20 intermediate grindings/cold pressing cycles to 574 h with 43 intermediate grinding/cold-pressing cycles, below 1070°C to synthesize single phase stoichiometric and off stoichiometric  $\text{Eu}_2\text{Ir}_2\text{O}_7$  respectively. In spite of such prolonged sinterings, minor traces of impurities were seen [7]. Hence the sintering protocol can affect the  $\text{IrO}_2$  losses, thus effecting the final stoichiometry and unit cell volume, which may result in anomalies in the sign of  $\frac{d\rho}{dT}$ . Because of these reasons, methods which minimize the sintering steps and reduce the sintering duration may be adopted to reduce  $\text{IrO}_2$  losses.

A wet chemical synthesis route for  $\text{Y}_2\text{Ir}_2\text{O}_7$  commonly known as the pechini method has been reported where mixing of precursors is carried out in deionized water with a chelating agent citric acid from which single phase product is obtained within 24 h of sintering. [10]. Synthesis through Pechini method and physical characterization has not been carried out so far for any lanthanide pyrochlore iridate ( $\text{A}_2\text{Ir}_2\text{O}_7$ ) samples. Hence the synthesis of  $\text{A}_2\text{Ir}_2\text{O}_7$  for all the atoms in lanthanide series would be new and comparison of its physical properties with the samples synthesized by solid state reaction technique would be interesting.

In the present work initially  $\text{Sm}_{1\pm x}\text{Ir}_{1\mp x}\text{O}_7$  [SmIO] ( $x = 0.02, 0.04$ ) samples were synthesized through solid state reaction technique to study the effect of stuffing on the slope of  $\rho$  versus T above  $T_{MI}$ . Later on a wet-chemical method of synthesis was carried out for five samples of  $\text{Ln}_2\text{Ir}_2\text{O}_7$  ( $A = \text{Pr}, \text{Sm}, \text{Gd}, \text{Dy}, \text{Er}, \text{Yb}$ ).  $\text{Pr}_2\text{Ir}_2\text{O}_7$  shows no transition down to 0.3 K, where as  $\text{Sm}_2\text{Ir}_2\text{O}_7$ ,  $\text{Gd}_2\text{Ir}_2\text{O}_7$ ,  $\text{Dy}_2\text{Ir}_2\text{O}_7$ ,  $\text{Er}_2\text{Ir}_2\text{O}_7$ ,  $\text{Yb}_2\text{Ir}_2\text{O}_7$ ,  $\text{Y}_2\text{Ir}_2\text{O}_7$  shows transitions at 117K, 124K, 134K, 140K, 130K, 155K respectively.

# Chapter 2

## Pyrochlore structure

Pyrochlore structure has a general formula  $A_2B_2O_7$  with generally the A site occupied by a rare earth ion and the B site ion occupied by a 3d/4d/5d transition metal ion. The oxidation state of A site ion is either 3+/4+ and B site ion 2+/5+. The space group of the ideal pyrochlore structure is Fd3m and there are eight molecules per unit cell. There are two non equivalent oxygen anions namely 8b and 48f. The A cation are eight coordinated and the B cation six coordinated. The A cation connects to six equally spaced oxygen ions (48f) and two oxygen ions (8b) at a slightly shorter distance from the central cations. The direction along which the cube is compressed is the [111] direction, along the 8b oxygen anions connecting the A cation, thus it forms a scalenohedra compressed along its diagonal. The smaller B cations are six coordinated and are located in the center of an octahedra with all the six oxygen ions (48f) at equal distances from the central cations (Fig 1 (a))<sup>[5]</sup>.

In this structure the only variable parameters are the unit cell edge length (a), and the x-coordinate of the oxygen ion at the 48f site (x, 0.125, 0.125). The value of x ranges from 0.3125 to 0.375. The shape of coordination polyhedra of A and B ions changes with change in 48f oxygen parameter x. Coordination around B becomes a regular octahedron for x=0.3125 and for x=0.375 the coordination around A becomes a regular cube.

The structure can also be explained as inter penetrating network of corner shared tetrahedra. The A cations forms a tetrahedra with 8b oxygen anion occupying the tetrahedral void. The B cations form a tetrahedra with an empty tetrahedral void. The A and

B kagome sublattices are separated by half fractional coordinate and they align along the  $[111]$  direction.

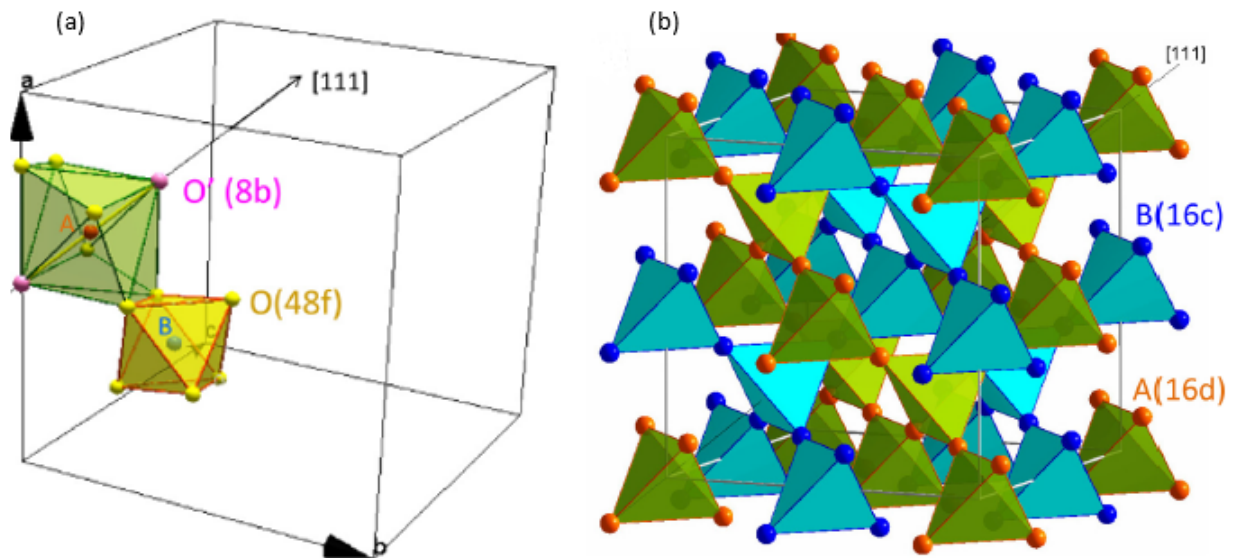


Figure 2.1: Pyrochlore structure

The spins occupying the corners of tetrahedra in the pyrochlore structure may give rise to geometrical frustration. It is not possible to minimize the interaction energy for all lattice sites at the same time. Typically a geometric frustration results in degenerate manifold of ground states rather than a single stable ground state configuration, leading to magnetic analogues of spin ice, spin liquid etc. Not surprisingly even slight perturbations induce instabilities in such system. The issue of how geometric frustration effects the ground states of strongly correlated pyrochlore systems leading to novel electronic properties is yet to be solved. In the case of 4d and 5d transition metal, pyrochlore oxides frustration leads to novel transport properties such as the anomalous Hall effect in  $\text{Nd}_2\text{Mo}_2\text{O}_7$  [11] and  $\text{Pr}_2\text{Ir}_2\text{O}_7$  [12], superconductivity in  $\text{Cd}_2\text{Re}_2\text{O}_7$  [13] and  $\text{AOs}_2\text{O}_6$  ( $A = \text{K}, \text{Rb}, \text{and Cs}$ ) [14], and the metal-insulator transition (MIT) in  $\text{Cd}_2\text{Os}_2\text{O}_7$ ,  $\text{Ln}_2\text{Ir}_2\text{O}_7$  ( $\text{Ln} = \text{Nd}, \text{Sm}, \text{Eu}$ ) [2], [6].

# Chapter 3

## Pyrochlore iridates

In the pyrochlore oxides with a 5d transition metal ion (e.g., Ir<sup>4+</sup>) at the B site, presence of a relativistic spin-orbit(SO) interaction term in the Hamiltonian gives rise to novel topological phases not present in their 3d and 4d analogs. For this reason, the iridates of the pyrochlore structure have gained significant attention in the recent years<sup>[7]</sup>. Phase diagram for 5d TMOs, depending on the strength of spin orbit coupling (SOC)  $\lambda$  and Coulomb repulsion  $U$  is shown in figure 3.1.

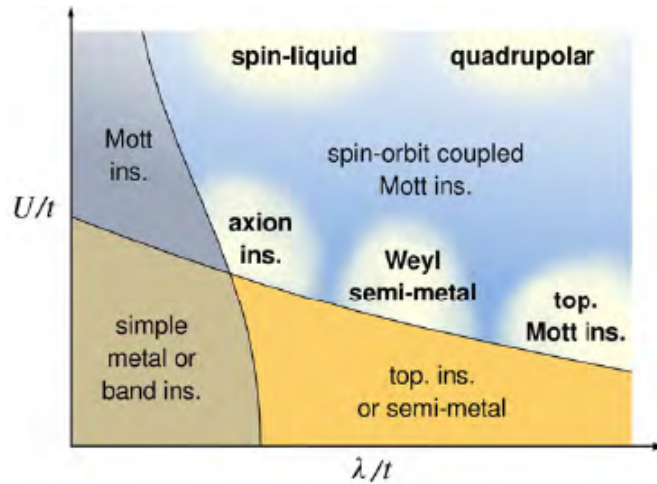


Figure 3.1: A schematic phase diagram showing various ground states depending on the strength of spin orbit coupling (SOC)  $\lambda$  and Coulomb repulsion  $U$  <sup>[1]</sup>

. The x and y axis are normalized by the hopping integral  $t$ .

The Weyl semimetallic (WSM) phase resides in the phase diagram where on site coulomb repulsion  $U$  and spin orbit coupling  $\lambda$  is comparable. Pyrochlore materials are



predicted candidate materials to realize the WSM phase<sup>[15]</sup>. Weyl semimetals are often

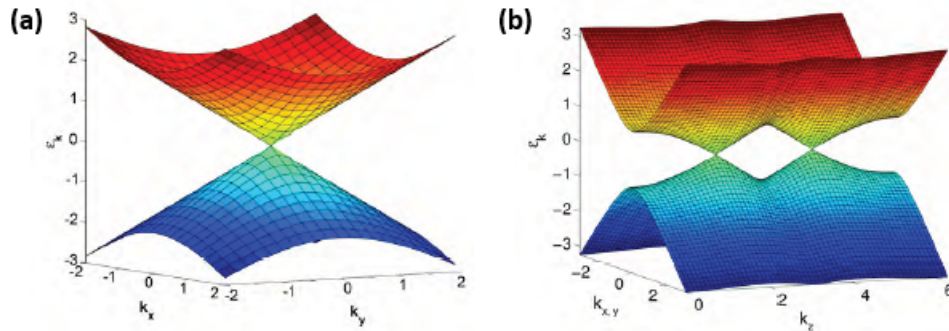


Figure 3.2: (a) dirac node, (b) pair of weyl nodes

considered as the 3d analogue of graphene. The special physics that happens in graphene is strongly coupled with its special band structure. The Fermi energy for the ground state is located at a point called the Dirac point where the minima of conduction band and maximum of valence bands touches. The conical shape of the band structure at these Dirac points lead to the name Dirac cone. The linear dispersion leads to electrons behaving like massless particles in that very region, comparable to photons but with a lower speed<sup>[15]</sup>. In Weyl semimetal the points where valence band and conduction band touch each other are not called Dirac nodes but Weyl nodes. Breaking of time reversal symmetry is necessary to realize a Weyl semimetal phase. The four spin in the corners of Ir tetrahedra undergo AFM ordering with spins arranged in an all-in all-out (AIAO) pattern thus time reversal symmetry is broken. For a Dirac cone, the nodes are on the surface, whereas for WSM, an even number of nodes are present as pairs, in the bulk. These nodes are objects with a definitive chirality<sup>[16]</sup>. For WSM phase  $\rho = \rho_0 T^{-n}$ .

As mentioned earlier  $\text{Ir}^{4+}$  in  $\text{A}_2\text{Ir}_2\text{O}_7$  is octahedrally coordinated. Therefore under crystal field splitting, 5d electrons fill in the three low-energy  $t_{2g}$  orbitals leaving the two high energy  $e_g$  orbitals unoccupied. The  $t_{2g}$  orbitals further split under the spin-orbit coupling into a  $j=3/2$  quadruplet and  $j=1/2$  doublet. The  $j=3/2$  level is completely filled, leaving the  $j=1/2$  level occupied by a single electron resulting in an effective spin  $1/2$  <sup>[4]</sup>. Below the magnetic order temperature, in an  $J_{\text{eff}}=1/2$  orders in AIAO pattern as discussed above<sup>[17]</sup>.

Pyrochlore iridates ( $\text{A}_2\text{Ir}_2\text{O}_7$ ), with  $\text{A} = \text{Nd}, \text{Sm}$  and  $\text{Eu}$  show a thermally induced metal to insulator transition at  $T_{MI}$ . The onset of insulating behavior is concomitant

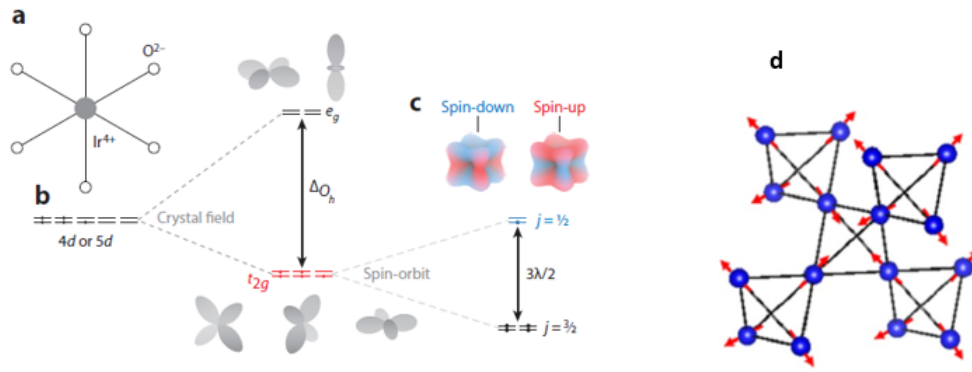


Figure 3.3: (a)(b)(c) Energy level splitting of 5d orbitals under octahedral field symmetry and spin orbit coupling, (b) All in all out ground state in  $\text{Ir}^{4+}$

with anti-ferromagnetic ordering of  $\text{Ir}^{4+}$  moments at  $T_N$  [7]. Considering the pyrochlore general formula  $\text{A}_2\text{B}_2\text{O}_7$ , for all the sample represented in the phase diagram in the figure 3.4 (a,b), where the B site is occupied by  $\text{Ir}^{4+}$  ion. This indicates that with the change in A site ionic radius (A site being a lanthanide ion) the physical property changes from metallic to insulating. There have been a large number of studies on the pyrochlore titanates on the correlation of physical properties with changes in stoichiometry through stuffing. On the other hand similar studies are lacking for the pyrochlore iridates.

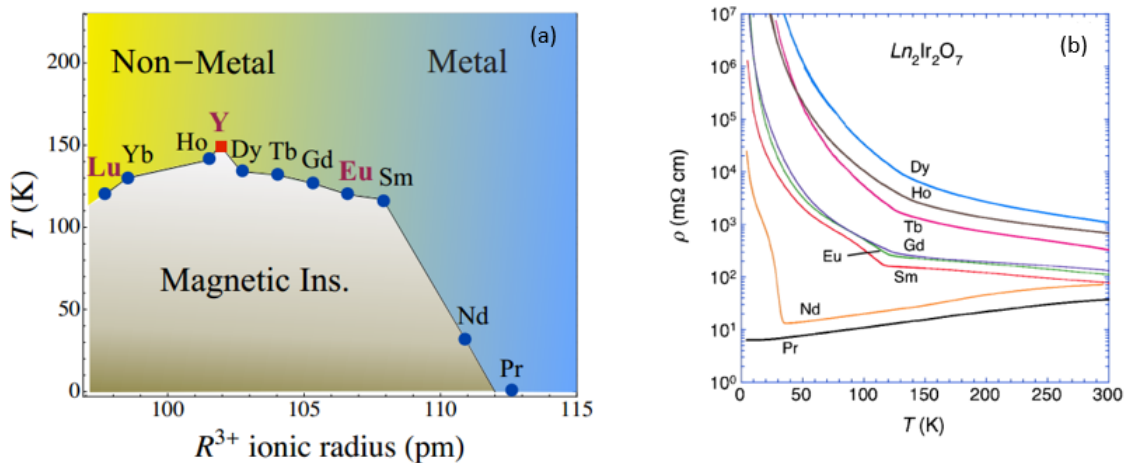


Figure 3.4: (a) Phase diagram and (b) electrical resistivities of  $\text{A}_2\text{Ir}_2\text{O}_7$  ( $\text{A} = \text{Pr}, \text{Nd}, \text{Sm}, \text{Eu}, \text{Gd}, \text{Tb}, \text{Dy}, \text{Ho}, \text{Y}$ )

# Chapter 4

## Experimental techniques

In this chapter the techniques used for structural as well as the physical property characterization will be discussed. The structural analysis was done using X-Ray diffraction technique and field-emission Scanning Electron Microscope (SEM). The specific heat, magnetic susceptibility and resistivity measurements were carried out using a Physical Property Measurement System (PPMS) from Quantum design, USA.

### 4.1 X-ray diffraction

Powder X-ray diffraction (XRD) is a routine technique used to analyse the structure of crystalline materials. It is based on the principle of constructive interference of X-rays scattered by crystalline material. The periodic arrays of atoms in a crystal can be visualized in the form of atomic planes. If X-ray radiation is incident on them such that its wavelength is comparable to the distance between these planes, then the crystalline structure behaves like a 3 dimensional diffraction grating. The basic principle behind XRD is explained by Bragg's equation and the Bragg's diffraction condition is given by

$$2d\sin\theta = n\lambda$$

where  $\lambda$  is the wavelength of the incident X-ray,  $d$  is the distance between interatomic planes,  $\theta$  is the glancing angle and  $n$  is an integer representing the order of diffraction.

In this work room temperature powder X-ray diffraction studies of the samples

were performed with Cu-K $\alpha$  radiation within the  $2\theta$  range of  $10^\circ$  to  $90^\circ$ . The XRD pattern was taken in  $\theta - 2\theta$  scan mode. In this mode, a monochromatic beam of X-ray is incident on the sample at an angle of  $\theta$  with the sample surface. The detector motion is coupled with the X-ray source in such a way that it always makes an angle  $2\theta$  with the incident direction of the X-ray beam. The resulting spectrum is a plot between the intensity recorded by the detector versus  $2\theta$ .

## 4.2 Scanning electron microscopy

For SEM a focused beam of electrons is positioned on the sample of interest. The electrons from the beam interact with the sample, by imparting energy to electrons causing its ejection. These ejected electrons are called secondary electrons. Since they have relatively low energy, only secondary electrons generated near the sample surface can reach the detector. Thus electrons can give information about the topology of the surface. When the electrons of the sample occupy the levels left by the secondary electrons (transitions between energy levels) X-ray photons are emitted. As energy levels are the characteristic of the atoms, X-ray photons are characteristic wavelength of the atoms. Thus the spectrum of X-rays gives an indication of chemical composition of sample.

## 4.3 Physical Property Measurement System

The Physical Property Measurement System (PPMS) provides a flexible, automated low-temperature and magnet system that can perform a variety of experiments requiring precise thermal control. The temperature range is 2K to 300K and the magnetic fields are up to  $\pm 9$  Tesla. The PPMS consists of a super insulated Dewar that encloses a sample chamber which is surrounded by liquid Helium. The temperature of the sample chamber is controlled by means of a heater present at the base of the sample chamber. The magnetic fields are controlled using a superconducting coil immersed in liquid Helium. PPMS can be used for magnetic, electro-transport, or thermo-electric measurements. The unique open architecture of the PPMS allows the user to customize the basic PPMS version different measurement options, such as the AC measurement System option, heat capacity option, or ultra-low field option. All PPMS options are fully automated.

### 4.3.1 Transport property measurements

Resistivity of the samples were measured using a four probe system in the PPMS set up. Typically, for electrical transport measurements, a two probe method is used. In this method an electric current is passed through the sample and voltage drop across the two terminals are measured. The measured resistance will have contribution from the resistance from the leads. To eliminate this, the voltage and current terminals can be separated so that there are four terminals on the sample. The voltage terminals are placed in between the current terminals so as to exclude the voltage drop due to the contact resistance of the current terminals. Since a voltmeter has very high resistance, negligible current passes through it and hence the voltage drop due to the contact resistance of voltage terminals is low. This leads to measurement of a more accurate resistivity.

The sample was attached to the sample holder via GE Varnish, by sticking it on to the cigarette paper. Both GE Varnish and cigarette paper are electrically insulating and thus prevents shorting of sample with the base of the holder. Contacts were made by soldering one end of each of four gold wires on the sample holder and the other end attached on the sample using silver paste. The sample dimensions were measured using a vernier callipers and was manually entered in the program, so that the system automatically calculate the resistivity.

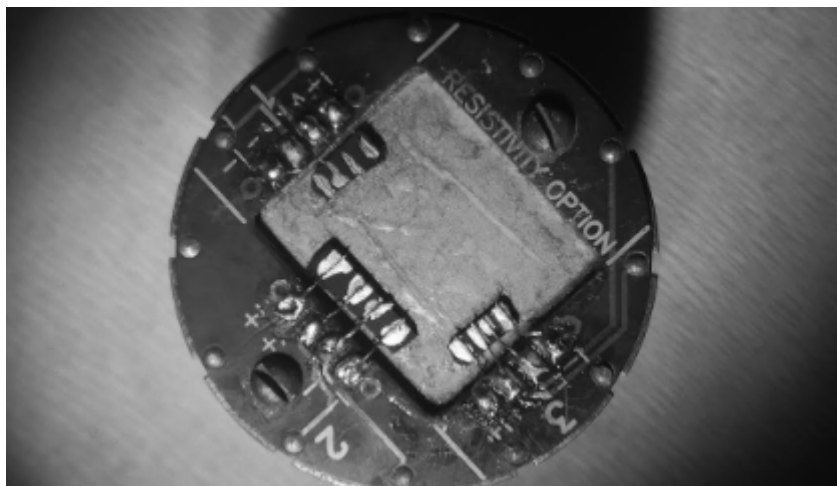


Figure 4.1: Image of the resistivity contacts made for measurement in PPMS

### 4.3.2 Magnetic property measurements

Magnetic measurements were carried out using a vibrating sample magnetometer (VSM) probe associated with the PPMS. Magnetization is measured as function of temperature under applied field. The sample is vibrated inside a coil of conducting wire at a fixed frequency. The resulting emf induced in the coil is proportional to sample's magnetic moment. The emf induced is amplified and then measured using the lock-in technique. Initially the sample was cooled from room temperature to 2K with zero applied field (ZFC), and the magnetization (measured in emu) was measured while warming up. Secondly the sample was again cooled from room temperature to 2K under applied field (FC) and magnetization was measured while warming up.

### 4.3.3 Heat Capacity measurements

Heat capacity is measured by controlling the heat provided to the sample and measuring the corresponding change in temperature. The sample is mounted on the sample holder by thin layer of Apiezon N grease. Before measuring the sample specific heat, addenda measurement is done with the layer of Apiezon N grease. Later the sample is mounted to measure the specific heat from which the addenda heat capacity is measured to obtain the sample heat capacity. High vacuum is a prerequisite for the measurements so that unaccounted heat losses via conduction can be minimized. Specific heat measurements were also done in the presence of magnetic field.

# Chapter 5

## **Sm<sub>2±x</sub>Ir<sub>2∓x</sub>O<sub>7</sub>, x=1, 0.04, 0.02 bulk material**

In this chapter, the preparation of polycrystalline Sm<sub>2±x</sub>Ir<sub>2∓x</sub>O<sub>7</sub> bulk samples and their structural characterization will be discussed. The first section deals with the synthesis of polycrystalline powder via a solid state reaction. The second section focuses on X-ray powder diffraction to study the structural properties. The last section summarizes the results.

### **5.1 Synthesis of samples**

Synthesis of iridate pyrochlores are highly tricky due to the loss of volatile IrO<sub>2</sub>. As IrO<sub>2</sub> tend to sublime at temperature approximately above 1050°C, the IrO<sub>2</sub> loss can be quite significant if the sample is not sintered for sufficient length of time at lower temperatures to allow for Sm<sub>2</sub>O<sub>3</sub> and IrO<sub>2</sub> to react. Moreover to prevent this loss sintering temperatures can be increased only in small increments. Further difficulty, specific to the synthesis of Sm<sub>2</sub>Ir<sub>2</sub>O<sub>7</sub> is related to the fact that, for annealing temperature higher than 1080°C the formation of phase Sm<sub>3</sub>IrO<sub>7</sub> is thermodynamically favoured.

Five different samples consisting of nominal compositions Sm<sub>2.04</sub>Ir<sub>1.96</sub>O<sub>7</sub>, Sm<sub>1.96</sub>Ir<sub>2.04</sub>O<sub>7</sub>, Sm<sub>2.02</sub>Ir<sub>1.98</sub>O<sub>7</sub>, Sm<sub>1.98</sub>Ir<sub>2.02</sub>O<sub>7</sub>, Sm<sub>2</sub>Ir<sub>2</sub>O<sub>7</sub> labelled as A1, A2, B1, B2, C respectively were synthesized using the solid-state reaction technique using precursors Sm<sub>2</sub>O<sub>3</sub> and IrO<sub>2</sub>. The samples were ground and sintered as two batches, the first batch consisting of A1

and A2, and second batch consisting of B1, B2 and C. A1 and A2 were sintered for 648 h with several intermediate grinding and cold pressing cycles below  $1070^\circ\text{C}$  starting from  $850^\circ\text{C}$  by increasing the temperature in steps of  $20^\circ\text{C}$ . Mechanical milling was also tried to mix  $Sm_2O_3$  and  $IrO_2$ ; however this method was discontinued due to precursor loss which tends to bound strongly to the walls of the vibrator as well as to the stainless steel balls which could not be retrieved. Thus sample C along with B1 and B2 were also synthesized by solid state reaction, with a sintering duration of 312 h below  $1070^\circ\text{C}$  starting above  $970^\circ\text{C}$  was carried out by increasing the temperature in steps of  $20^\circ\text{C}$ .

## 5.2 Structural characterization of samples

The samples prepared were thoroughly characterized using powder X Ray diffraction. Figure 5.1 shows the XRD data of various  $Sm_{2\pm x}Ir_{2\mp x}O_7$  samples.

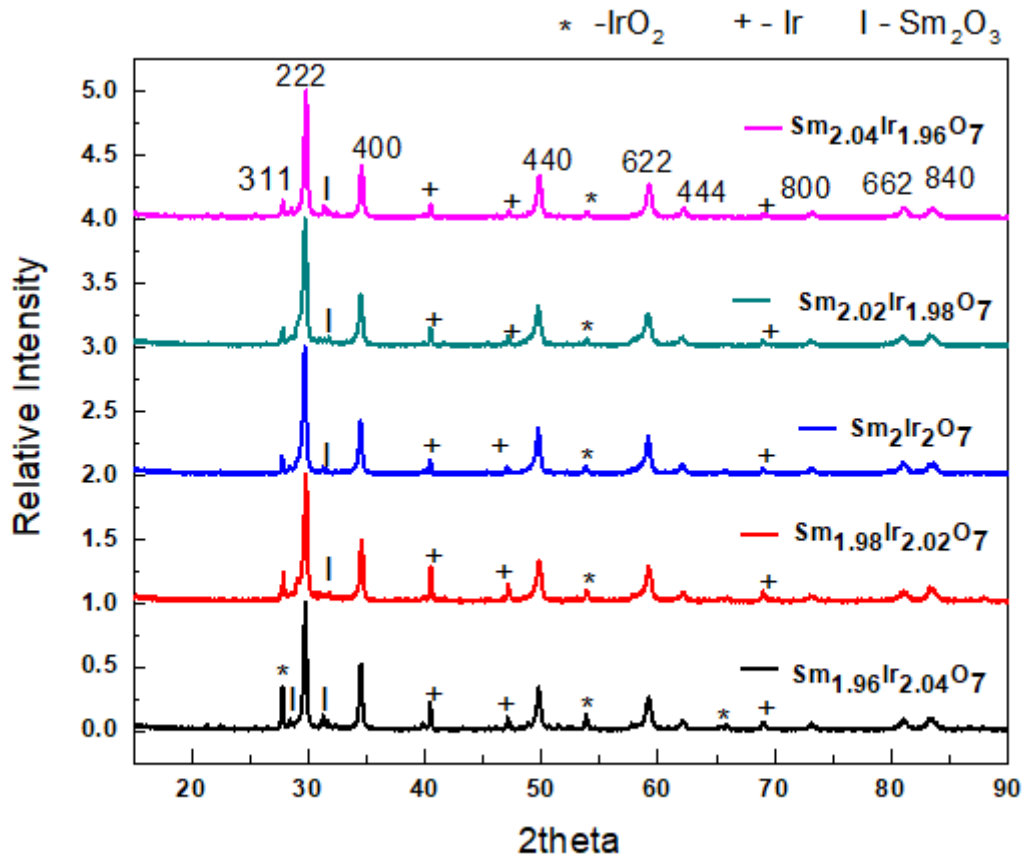


Figure 5.1: X Ray diffraction pattern for  $Sm_{2\pm x}Ir_{2\mp x}O_7$ , ( $x= 0, 0.02, 0.04$ )

From the X Ray diffraction patterns for  $Sm_{2\pm x}Ir_{2\mp x}O_7$ , ( $x=0, 0.04, 0.02$ ) (Fig 3)



it is evident that even after sintering for a duration of about 312 h for  $Sm_{2.02}Ir_{1.98}O_7$ ,  $Sm_{1.98}Ir_{2.02}O_7$ ,  $Sm_2Ir_2O_7$  and 648 h for  $Sm_{2.04}Ir_{1.96}O_7$ ,  $Sm_{1.96}Ir_{2.04}O_7$ , along with the formation of pyrochlore phase significant traces of  $IrO_2$ , Ir metal and minor traces of  $Sm_2O_3$  were present. The  $IrO_2$  peak intensity for  $Sm_{1.98}Ir_{2.02}O_7$ , and  $Sm_{1.96}Ir_{2.04}O_7$  samples were greater compared to other samples, which may be due to the excess  $IrO_2$  taken to produce the off stoichiometry, which however remained unreacted. All the pyrochlore diffraction peaks could be indexed based on  $Fd3m$  space group and the impurity phases were discernible due to their large relative intensity.

Figure 5.2 represent the X Ray Diffraction pattern for  $Sm_{2.04}Ir_{1.96}O_7$  where the  $IrO_2$ , Ir and  $Sm_2O_3$  impurity peaks are clearly evident.

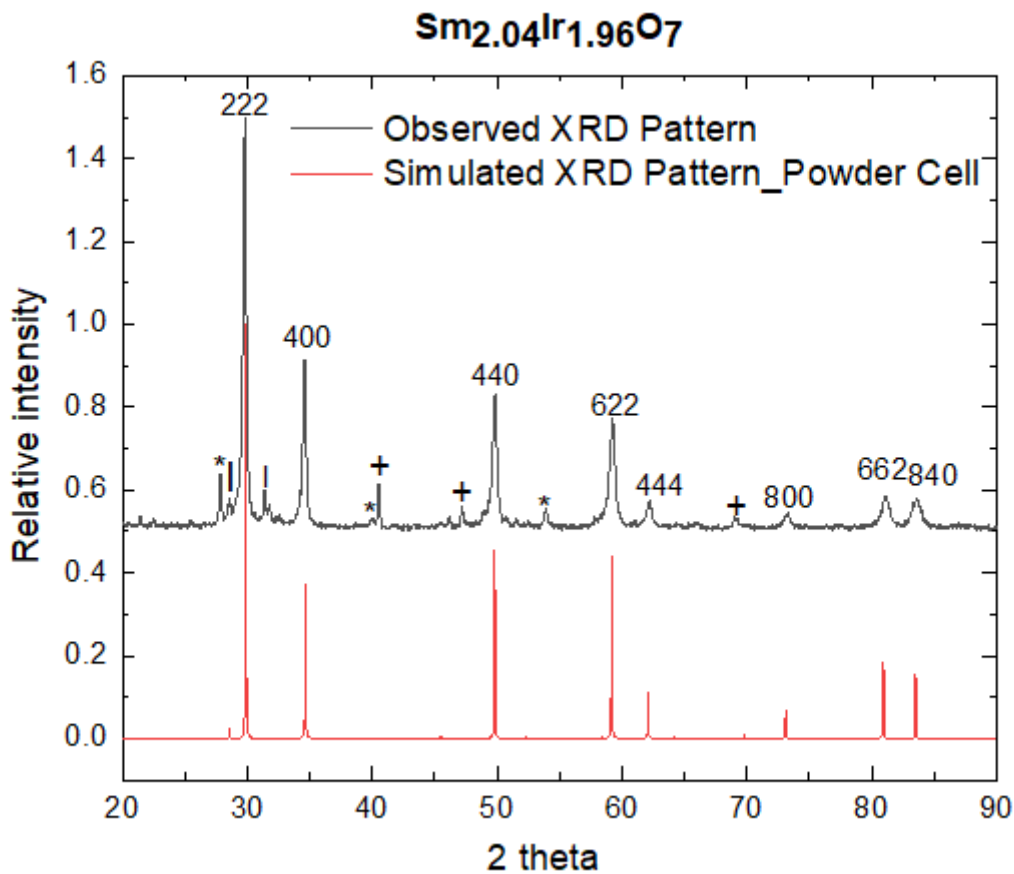


Figure 5.2: Simulated and observed X Ray diffraction pattern for  $Sm_{2.04}Ir_{1.96}O_7$

From the XRD, it could be concluded that the sample kept for longer sintering duration i.e 648 h for  $Sm_{2.04}Ir_{1.96}O_7$  had less intense  $IrO_2$  peaks. Comparatively high intensity impurity peaks for  $Sm_{1.96}Ir_{2.04}O_7$  might be due to the excess  $IrO_2$  taken, which is even present in  $Sm_{1.98}Ir_{2.02}O_7$ , sintered for 312 h.

### 5.3 Summary and Conclusions

The X Ray diffraction patterns show the formation of pyrochlore phase along with significant traces of impurity phases. Even after multiple steps of sintering and cold pressing cycles, the desired single phase was not obtained. A method which minimize the number of sintering steps, so as to prevent  $IrO_2$  loss, at the same time to obtain single phase of pyrochlore, has to be adopted.

# Chapter 6

## $A_2Ir_2O_7$ , $A = Pr, Gd, Sm, Dy, Er, Yb$

In this chapter, the preparation of polycrystalline  $A_2Ir_2O_7$ ,  $A = Pr, Gd, Sm, Dy, Er, Yb$  bulk samples as well as their structural characterization will be discussed. The first section deals with the importance of synthesis of polycrystalline powder via wet chemical route. The second section focuses on the synthesis methods. Later on the structural characterization of synthesized  $A_2Ir_2O_7$  samples will be discussed and compared with the results obtained for sample synthesized via solid state reaction technique. The results are summarized in the last section.

### 6.1 Wet chemical synthesis route for Pyrochlore iridates

In Chapter 5, we elaborated on the need for a better synthesis procedure to synthesize pyrochlore iridates. Standard solid-state techniques for processing separate precursor powders can approach homogeneity in the final product only after many grinding and sintering steps. A wet chemical synthesis route for  $Y_2Ir_2O_7$  commonly known as the pechini method has been recently reported where mixing of precursors is carried out in deionized water with a chelating agent citric acid for 6 h and annealed after drying for 12 h at 1000°C from which single phase product is obtained [18].

Wet chemical synthesis route via Pechini method would be an efficient way to prevent  $IrO_2$  losses because a 12 to 24 hrs sintering duration is expected to be sufficient to

obtain a single phase. sample. Synthesis of  $A_2Ir_2O_7$  where A is an atom in the lanthanide series using this method has not been reported so far. Hence the synthesis of  $A_2Ir_2O_7$  for the members of lanthanide series would be new and comparison of its physical properties with the samples synthesized by solid state reaction technique would be interesting.

### 6.1.1 Synthesis of bulk samples

For wet chemical synthesis, the precursors used were nitrate hydrate of A atom ( $A = Pr, Sm, Gd, Dy, Er, Yb$ ) and  $IrCl_3 \cdot xH_2O$ . Precursors were added to deionized water along with citric acid and was heated and stirred at  $80^\circ C$  for 5 h after which the mixture was dried by raising the temperature. The solid was ground to powder and kept for sintering for 4 h at  $800^\circ C$ , and 6 h at  $1000^\circ C$ . The sample was pelletized and sintered at  $1000^\circ C$  for 12 h. The flowchart of the synthesis route is given in Figure 6.1.

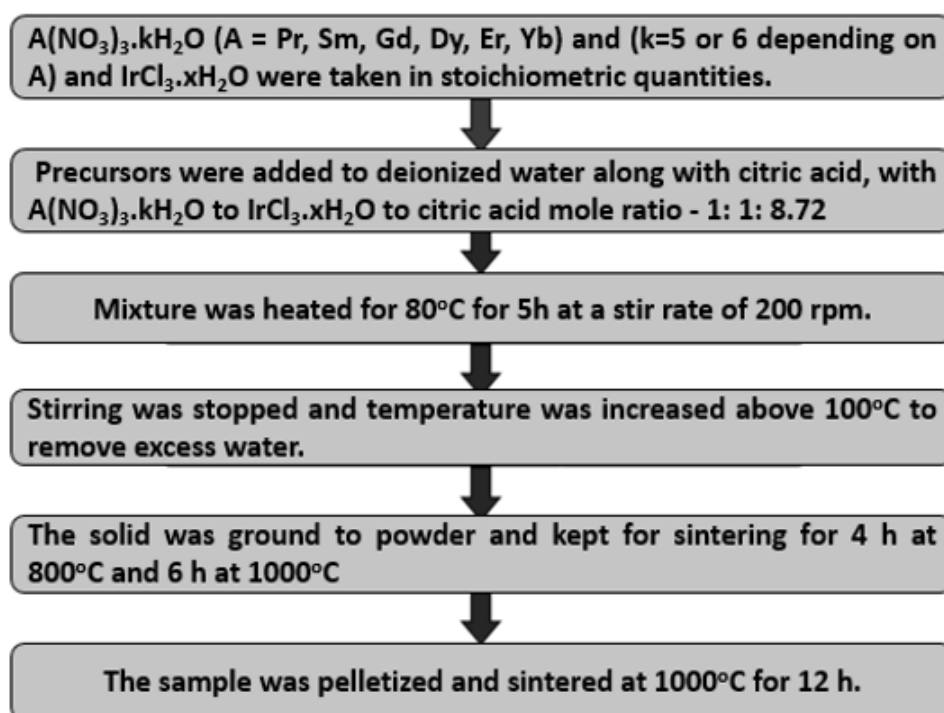


Figure 6.1: Wet chemical synthesis route for  $A_2Ir_2O_7$ ,  $A = Pr, Sm, Gd, Dy, Er, Yb$

### 6.1.2 Structural characterization of the samples

Figure 6.2 shows the X Ray diffraction pattern for  $A_2Ir_2O_7$ , ( $A = Pr, Sm, Gd, Dy, Er, Yb$ ). Except for  $Pr_2Ir_2O_7$ , in all the other scans no significant traces of precursors are

seen. The relative intensity of any impurity peaks present may be very less compared to the pyrochlore peaks. The variation in lattice parameter on the radius of  $A^{3+}$  ion is depicted in Figure 6.3. The lattice parameter is extracted using the UnitCell software decreases with decrease in ionic radius of  $A^{3+}$  ion as expected. This trend in lattice parameter was confirmed with the rightward shift in peak position of [222] from  $Pr_2Ir_2O_7$  to  $Yb_2Ir_2O_7$  as shown in panel b.

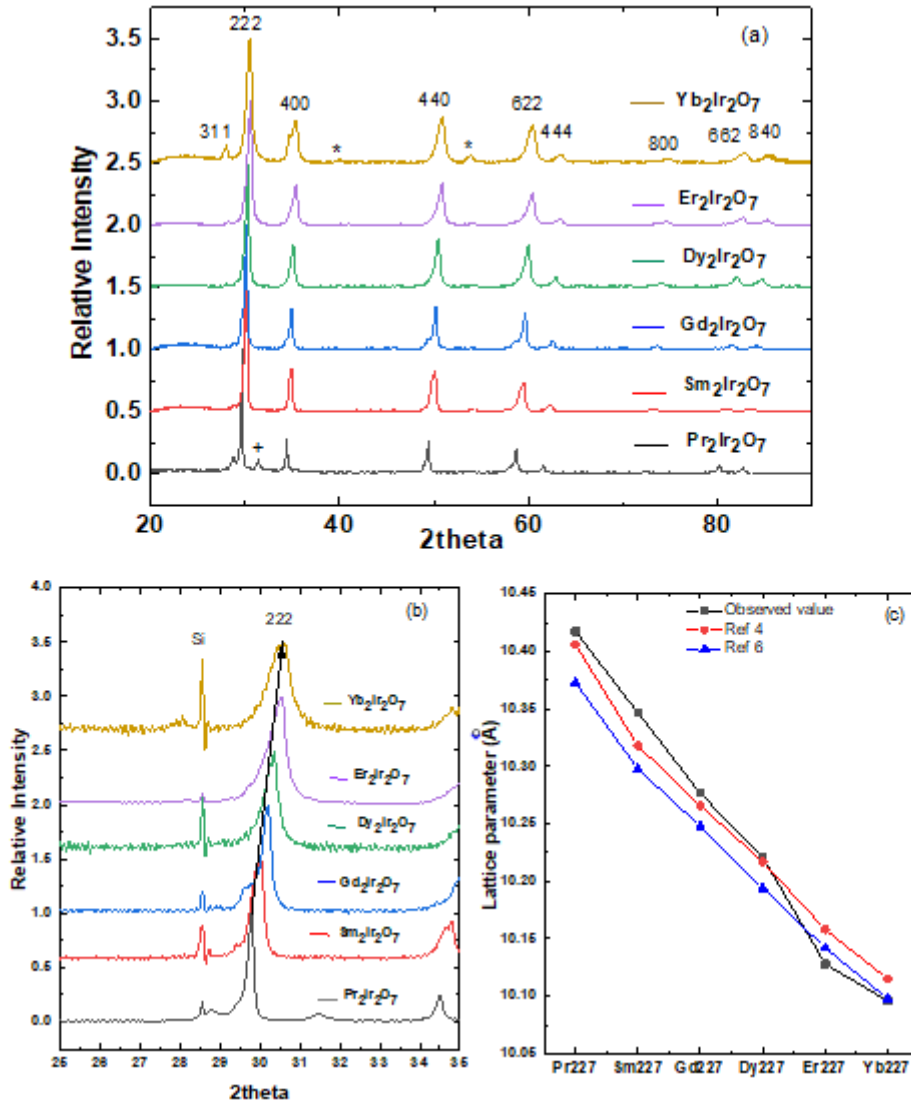


Figure 6.2: X Ray diffraction pattern, [222] Peak shift and lattice parameter variation for  $A_2Ir_2O_7$ ,  $A = Pr, Sm, Gd, Dy, Er, Yb$ .

Some representative SEM images of all the synthesized samples are shown in figure 6.3. On finding the particle size from FWHM, for all the samples synthesized

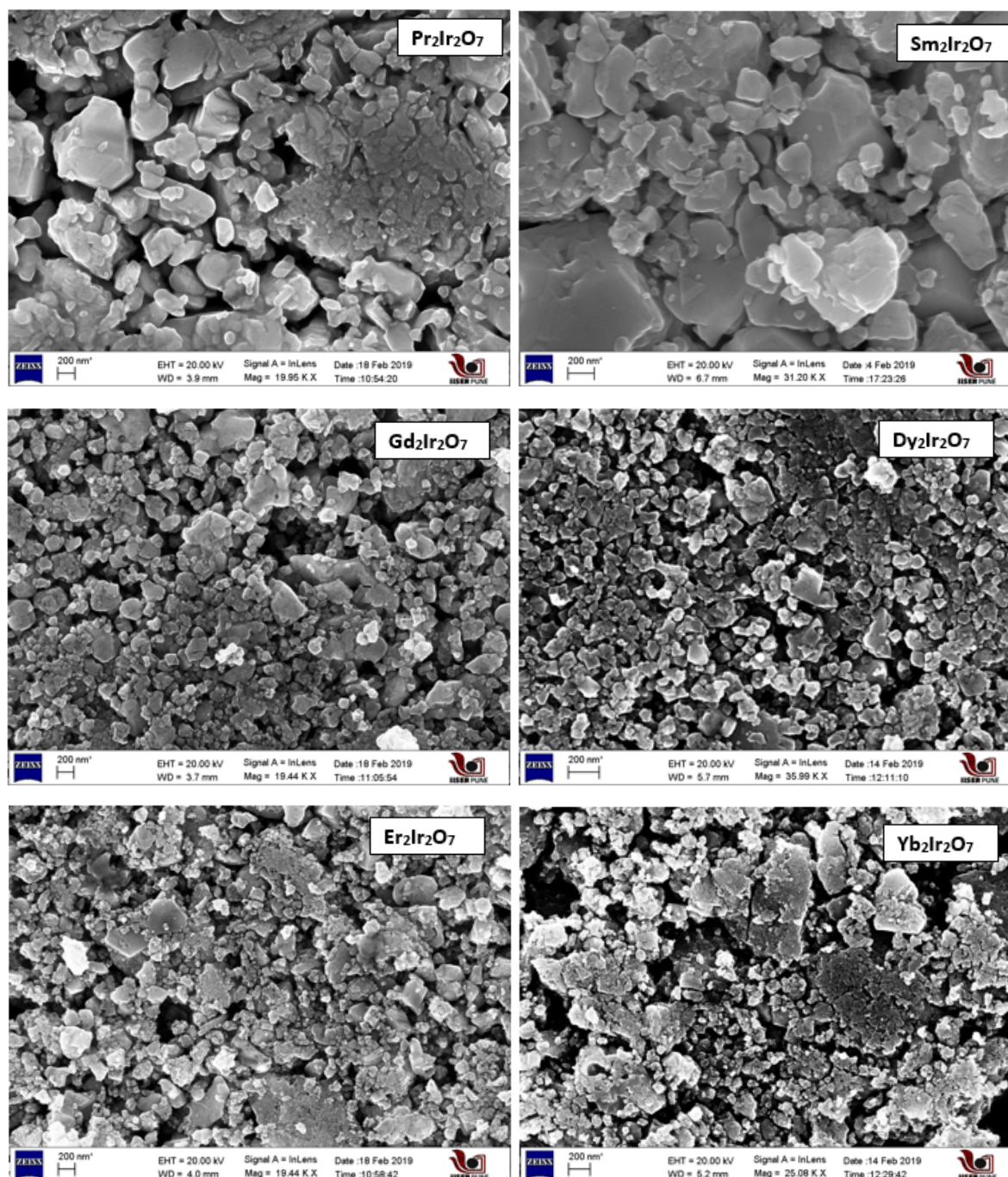


Figure 6.3: SEM images for  $Ln_2Ir_2O_7$ ,  $Ln=Pr, Sm, Gd, Dy, Er, Yb$

by wet chemical method the range lied below 100 nm. It was difficult to estimate the particle sizes from SEM images as the samples weren't homogeneous. For all the wet chemically synthesized samples, on finding the composition through EDX, the A/Ir ration was observed to be more than 1, around of 1.05. The ratio varied with the excitation

voltage. Sm227 sample showed the ratio close to 1 within the error bar at 20 KV, where as Gd227 at 15 KV. For each sample the excitation voltage has to be adjusted so that accurate values are obtained. The slight increase of A/Ir ratio above 1, might be due to the Ir precursor used which is  $\text{IrCl}_3 \cdot x\text{H}_2\text{O}$ . As the value of  $x$  wasn't known, there is always an error in stoichiometric weight of Ir precursor taken. On calculating the amount to be weighed, the molar mass of anhydrous  $\text{IrCl}_3$  was taken, as  $x$  is not known. Hence always a slightly deficient Ir precursor than required are taken for the reaction. A higher A/Ir ratio was observed on scanning a larger area, while ratio close to 1 was obtained on scanning small as well as clean areas.

### 6.1.3 Structural comparison of the samples synthesized via solid and wet chemical route

Figure 6.5 shows a comparison of the synthesis methods, the solid state reaction and the wet chemical route for  $\text{Sm}_2\text{Ir}_2\text{O}_7$ .

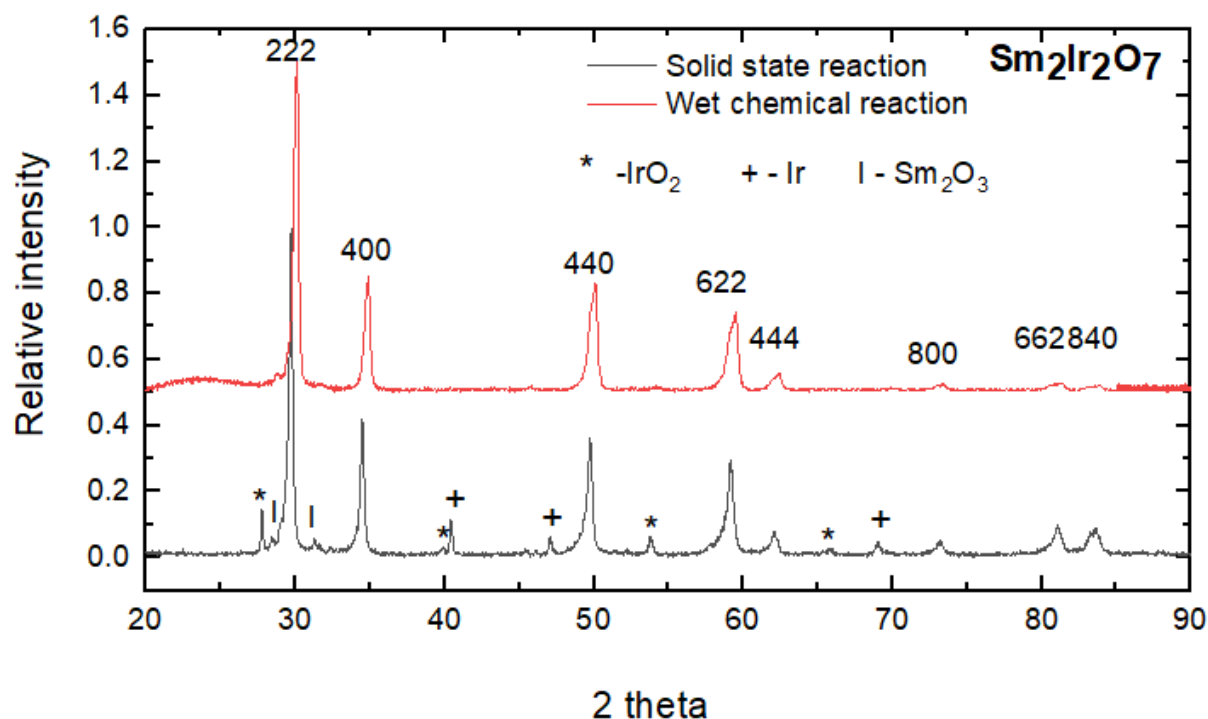


Figure 6.4: X ray diffraction pattern comparison for )  $\text{Sm}_2\text{Ir}_2\text{O}_7$  synthesized via solid state reaction and wet chemical reaction methods



From the figure it is clearly evident that the samples synthesized via solid state reaction method has significant impurity peaks compared to that of wet chemical reaction route. Compared to solid state reaction method which had a sintering duration of more than 330 hrs, wet chemical method had a sintering duration of less than a total of 48 hrs within which single phase was obtained. For wet chemical reaction method homogeneity of the precursors is reached in the initial stages where the mixing take place at atomic level in the deionized water. As a result multiple steps of grinding and sintering steps are not required. Moreover the minimized sintering steps results in reduced  $\text{IrO}_2$  loss, which is necessary to achieve the single phase.

Studies on Mott insulator  $\text{Sr}_2\text{IrO}_4$  reveals a contradiction in the physical properties of samples synthesized via solid state reaction technique and planetary ball milling, with the latter method having larger particle size and the results matching with studies of its single crystals. Ball milling is known to improve chemical reactions resulting in well mixed homogeneous mixture of precursors which is difficult to achieve manually<sup>[19]</sup>.

Similarly on comparing the two synthesis methods, there are fewer grains in the samples synthesized via the wet chemical route at the same scale length, indicating that atomic level mixing to achieve a homogeneous mixture increased the size of the crystal grains and reduced the number of grain boundaries.

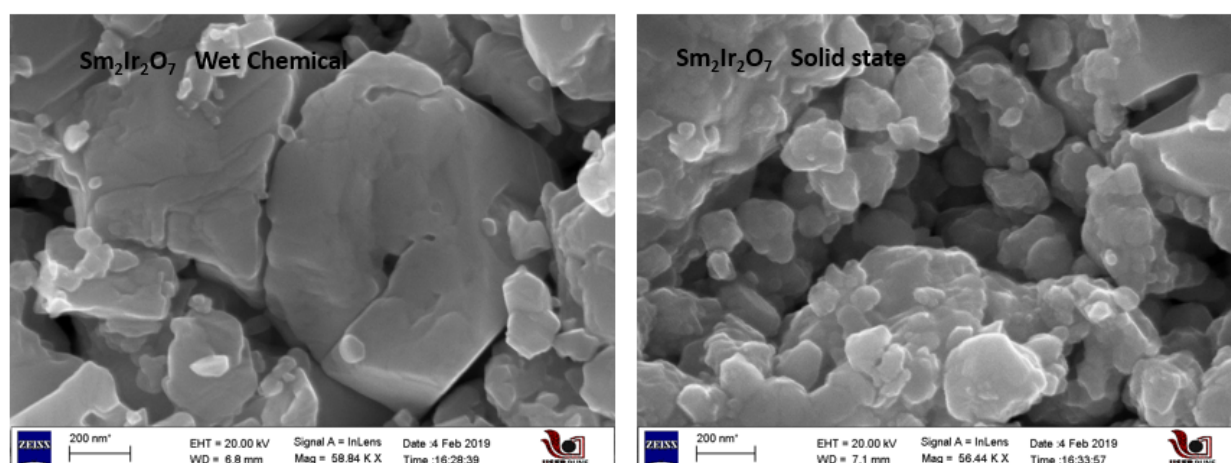


Figure 6.5: Microstructure comparison for  $\text{Sm}_2\text{Ir}_2\text{O}_7$  synthesized via solid state reaction and wet chemical reaction methods using SEM images



### 6.1.4 Summary and conclusion

Most of the pyrochlore iridate with A site occupied by lanthanide ion, reported in the literature are synthesized using the conventional ceramic route, which takes more than 600 hrs of sintering to stabilize the pyrochlore phase. We have been able to synthesize  $\text{Ln}_2\text{Ir}_2\text{O}_7$  ( $\text{Ln} = \text{Pr}, \text{Sm}, \text{Gd}, \text{Dy}, \text{Er}, \text{Yb}$ ) using a wet chemical technique through a single sintering. As the final stoichiometry can effect the physical properties, wet chemical route is a promising method, which minimizes off stoichiometry caused due to  $\text{IrO}_2$  losses, at the same time achieving single phase.

## 6.2 Physical Property Measurements

### 6.2.1 Electrical transport measurements

The resistivity measurements for all the samples were measured using PPMS. A plot of  $\rho(T)/\rho(300\text{K})$  versus temperature is shown in figure 6.6 and 6.7.

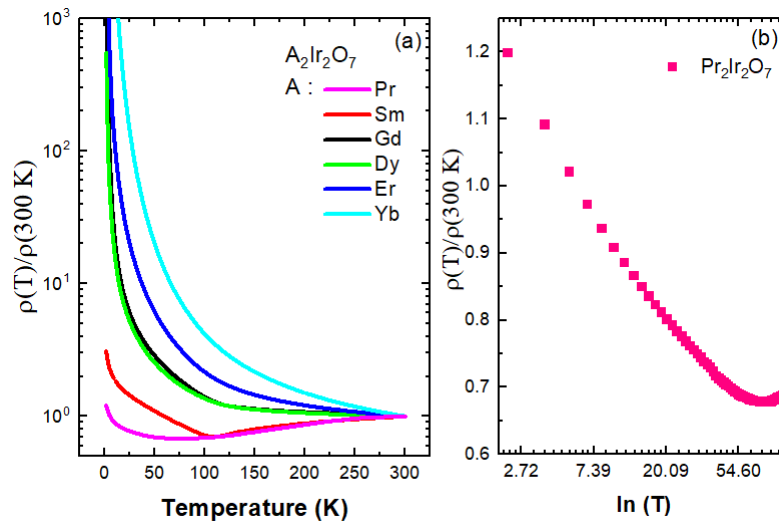


Figure 6.6: (a)  $\rho(T)/\rho(300\text{ K})$  for  $A_2\text{Ir}_2\text{O}_7$ , with  $A = \text{Pr}, \text{Sm}, \text{Gd}, \text{Dy}, \text{Er}, \text{Yb}$ , (b)  $\rho(T)/\rho(300\text{ K})$  versus  $\ln(T)$  plot for  $\text{Pr}_2\text{Ir}_2\text{O}_7$  in the temperature range 2K to 100K

The resistivity of  $\text{Sm}_2\text{Ir}_2\text{O}_7$ ,  $\text{Gd}_2\text{Ir}_2\text{O}_7$  shows a metal to insulator transition at 109 K and 121 K respectively and  $A_2\text{Ir}_2\text{O}_7$  with  $\text{Ln} = \text{Dy}, \text{Er}, \text{Yb}$  shows an insulating behaviour. The magnitude of the resistivity doesn't vary much with the literature values for the samples. A completely metallic behaviour is expected for  $\text{Pr}_2\text{Ir}_2\text{O}_7$ , but at low

temperature an upturn is observed. This upturn is attributed to the kondo effect which is shown in 6.6(b), where a linear behaviour of  $\rho$  versus  $\ln(T)$  is seen below 50 K. Kondo effect below 50 K has already been reported for  $\text{Pr}_2\text{Ir}_2\text{O}_7$  [20].

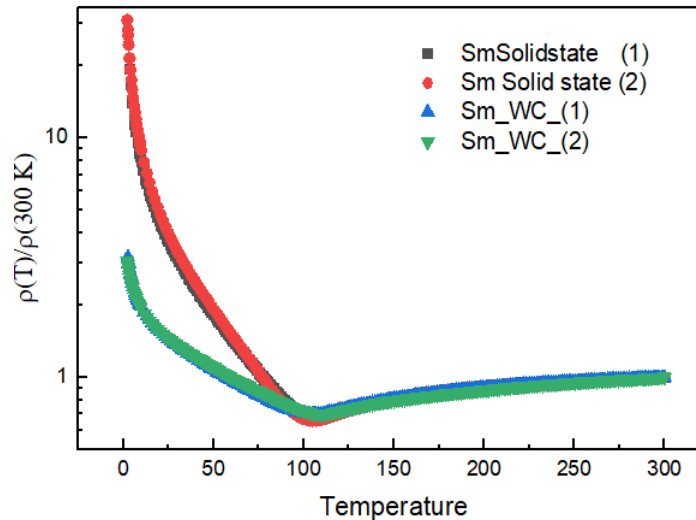


Figure 6.7:  $\rho(T)/\rho(300 \text{ K})$  for  $\text{Sm}_2\text{Ir}_2\text{O}_7$ , synthesized via solid state reaction and wet chemical method (WC). In the figure two samples each of  $\text{Sm}_2\text{Ir}_2\text{O}_7$ , for each synthesis method is shown. Wet chemical method was repeated for the sample to check the reproducibility. Resistivity data for the two samples of the same compound synthesized at two different times via solid state method, to compare its low temperature magnitude with that of wet chemical method

Comparing the resistivity data for  $\text{Sm}_2\text{Ir}_2\text{O}_7$  synthesized via solid state reaction and wet chemical route it is seen that at lower temperature, the resistivity magnitude for sample synthesized via former method is higher. This correlates with the micro structure of images, in which sample synthesized via solid state method has large number of smaller grains, resulting in more number of grain boundaries, thus causing larger resistivity. All the  $\text{Sm}_2\text{Ir}_2\text{O}_7$  samples shows a metal to insulator transition which is concomitant with AFM ordering. The transition is not very sharp, and the observed transition temperature is 109 K, which is lower compared to the literature value 115 K. As a metal insulator transition is observed in the sample, the value of  $T_{MI}$  can be confirmed by measuring the magnetic susceptibility from which  $T_N$  can be measured

The resistivity data were fitted using four different models: arrhenius behaviour, variable range hopping with or without correlations, and power law. The arrhenius behaviour of resistivity is fitted using the formula  $\rho = \rho_0 \exp(\Delta/T)$ ,  $\Delta$  is the activation

energy. For a semiconductor or an insulator, the value of resistivity decreases with increasing temperature. At lower temperature the charge carriers cannot cross the energy gap to contribute to conduction. At higher temperature the thermal energy is sufficient to result in conduction, thus reducing the resistivity. The variable range hopping was fit using the formula  $\rho = \rho_0 \exp(\Delta/T)^{0.25}$ . The equation describes the resistivity behaviour at low temperatures for systems with localized charge carrier states. For example, in pyrochlore iridate with rare earth ion sitting in the A site, 4f. If the effect of exchange interactions between localized 4f electrons and itinerant 5d electrons are considered the resistivity behaviour may be fit using the formula  $\rho = \rho_0 \exp(\Delta/T)^{0.5}$ , where electronic correlations are considered. To check whether the sample is a weyl semi metal (WSM)  $\rho = \rho_0 T^{-n}$ , was used. The sample is confirmed to have WSM ground state, if  $n=1$  or  $4$ , where the former arises for a pristine system without any charged impurities, where the latter arises when the system contains charged impurities either intrinsic or doped.

Sample	Best fit
$\text{Pr}_2\text{Ir}_2\text{O}_7$	$\rho = \rho_0 T^{-n}$
$\text{Sm}_2\text{Ir}_2\text{O}_7$	$\rho = \rho_0 T^{-n}$
$\text{Gd}_2\text{Ir}_2\text{O}_7$	$\rho = \rho_0 e^{(\Delta/T)^{0.5}}$
$\text{Dy}_2\text{Ir}_2\text{O}_7$	$\rho = \rho_0 e^{(\Delta/T)^{0.5}}$
$\text{Er}_2\text{Ir}_2\text{O}_7$	$\rho = \rho_0 e^{(\Delta/T)^{0.5}}$
$\text{Yb}_2\text{Ir}_2\text{O}_7$	$\rho = \rho_0 e^{(\Delta/T)^{0.5}}$

The table represents the resistivity behaviour to which the sample most closely fitted. The resistivity plot for all the samples, with each fitted to four resistivity behaviours are shown from figure 6.8 to 6.13.  $\text{Pr}_2\text{Ir}_2\text{O}_7$  samples best fit to power law with the value of  $n$  being 0.19. The sample doesn't realize in a WSM ground state.

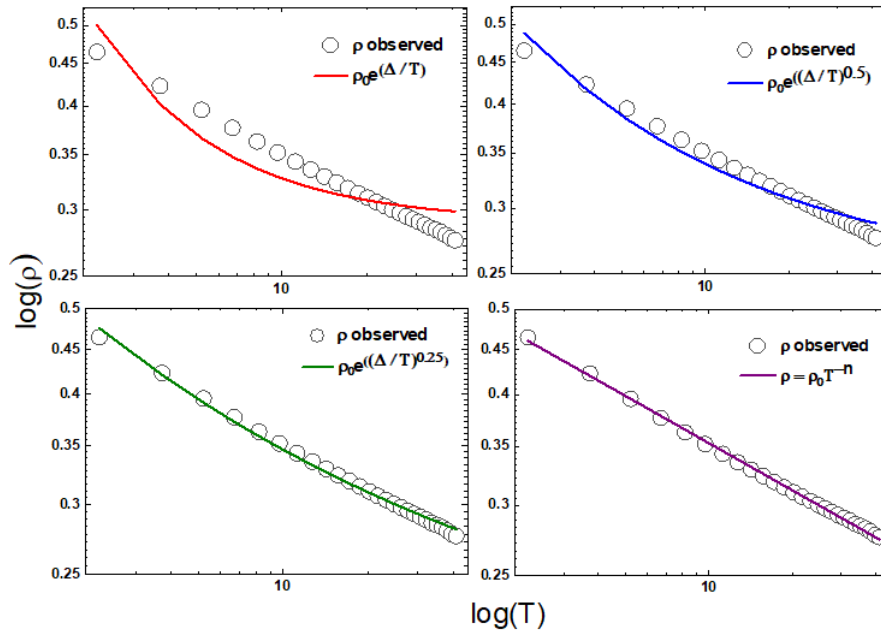


Figure 6.8: Resistivity versus temperature of  $\text{Pr}_2\text{Ir}_2\text{O}_7$ . The open black circles are the observed resistivity point. The solid red, blue, green and violet lines are best fits of the resistivity for arrhenius behavior, variable range hopping with electronic correlations, variable range hopping and power law.

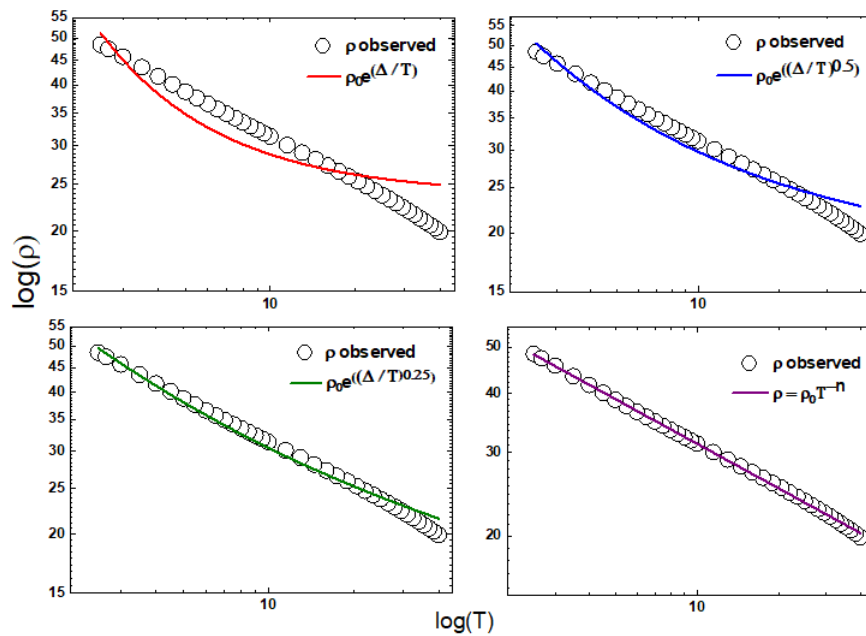


Figure 6.9: Resistivity versus temperature of  $\text{Sm}_2\text{Ir}_2\text{O}_7$ . The open black circles are the observed resistivity point. The solid red, blue, green and violet lines are best fits of the resistivity for arrhenius behavior, variable range hopping with electronic correlations, variable range hopping and power law.

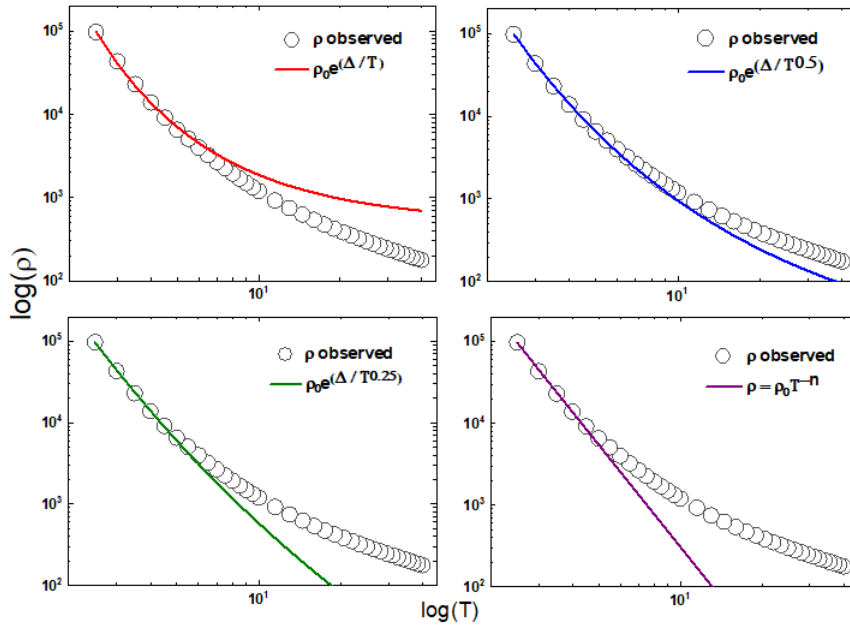


Figure 6.10: Resistivity versus temperature of  $\text{Gd}_2\text{Ir}_2\text{O}_7$ . The open black circles are the observed resistivity point. The solid red, blue, green and violet lines are best fits of the resistivity for arrhenius behavior, variable range hopping with electronic correlations, variable range hopping and power law.

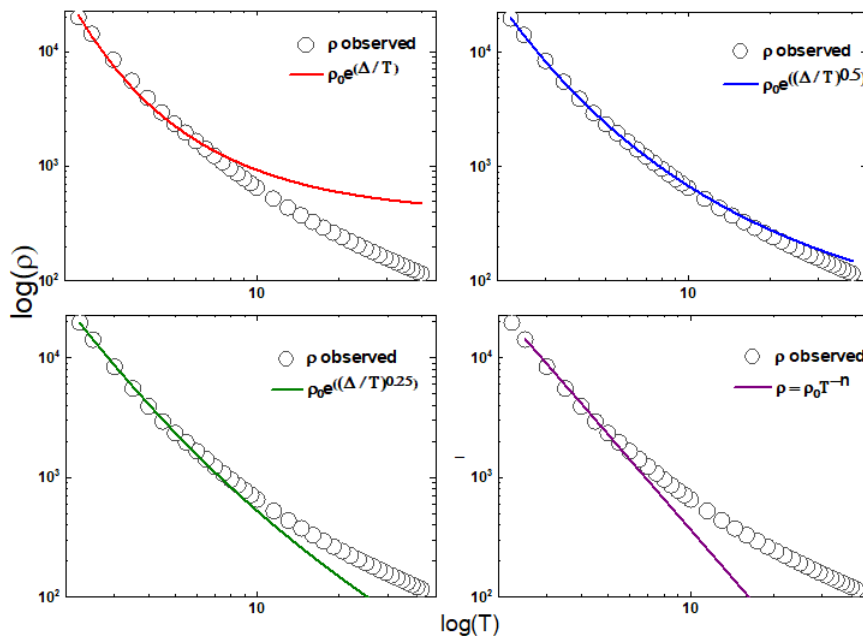


Figure 6.11: Resistivity versus temperature of  $\text{Dy}_2\text{Ir}_2\text{O}_7$ . The open black circles are the observed resistivity point. The solid red, blue, green and violet lines are best fits of the resistivity for arrhenius behavior, variable range hopping with electronic correlations, variable range hopping and power law.

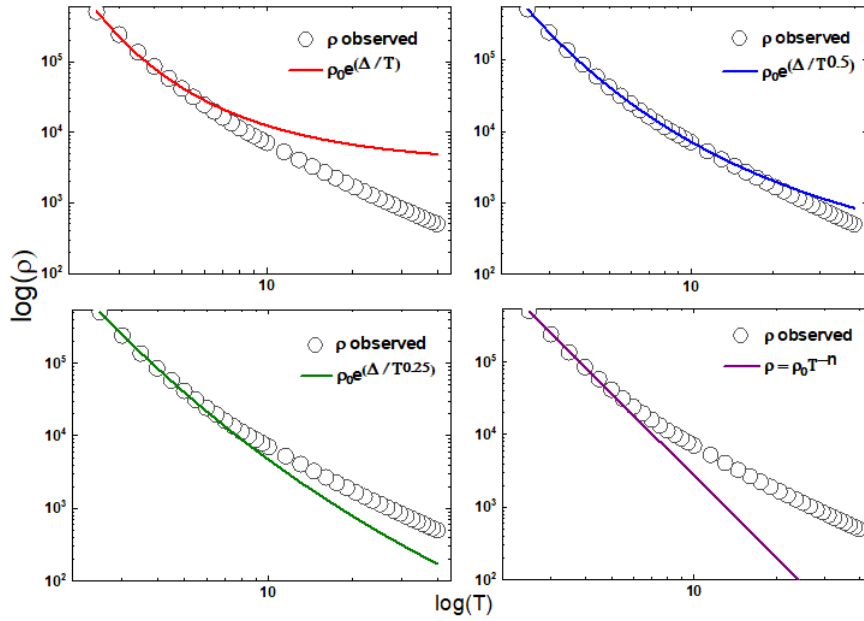


Figure 6.12: Resistivity versus temperature of  $\text{Er}_2\text{Ir}_2\text{O}_7$ . The open black circles are the observed resistivity point. The solid red, blue, green and violet lines are best fits of the resistivity for arrhenius behavior, variable range hopping with electronic correlations, variable range hopping and power law.

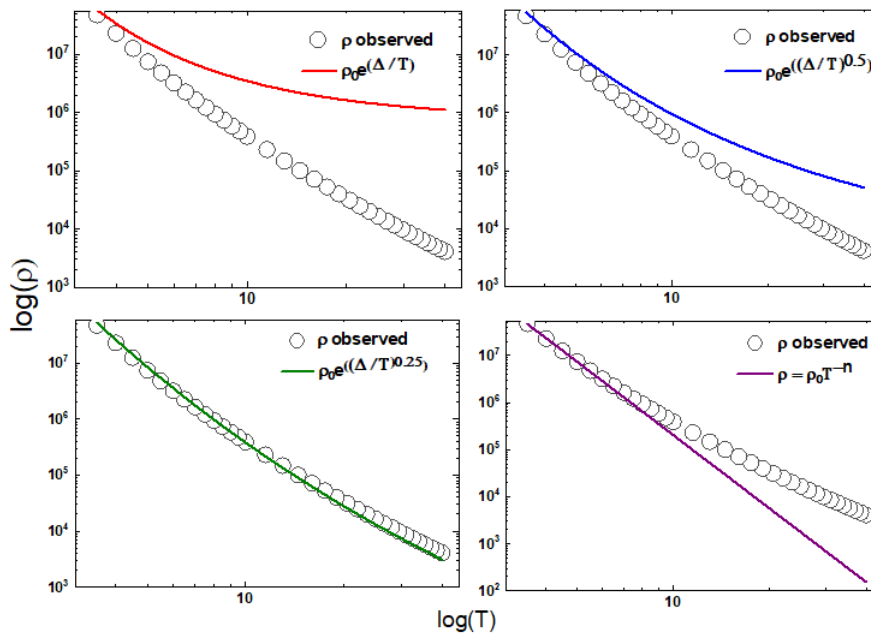


Figure 6.13: Resistivity versus temperature of  $\text{Yb}_2\text{Ir}_2\text{O}_7$ . The open black circles are the observed resistivity point. The solid red, blue, green and violet lines are best fits of the resistivity for arrhenius behavior, variable range hopping with electronic correlations, variable range hopping and power law.

## 6.2.2 Magnetic measurements

Temperature dependent field cooled and zero field cooled magnetization, in presence of applied magnetic field are shown (Fig 6.14, 6.15) for Sm227. In order to show the transition temperature clearly, reciprocal of magnetic susceptibility versus T was plotted. For Sm227, on cooling below room temperature, the  $\chi(T)$  linearly increased till  $T_N$ , where the Ir moments undergo all-in/all-out ordering (AFM ordering). The data below  $T_N$  show large ZFC-FC bifurcation. This bifurcation is believed to be due to presence of  $180^\circ$  domain walls. On considering Dy227 the ZFC-FC splitting is not clear compared to Sm227, Gd227, Er227 and Yb227. The reason might be the contribution of large magnitude moments of  $\text{Dy}^{3+}$ . Hence for Dy227  $T_N$  couldn't be found out. The obtained  $T_N$  values matches almost with the literature values for all the samples i.e for Sm227-118 K, Gd227-123 K, Er227-137 K, Yb227-129 K. Dy227 a clear splitting couldn't be observed which might be due to the large  $\text{Dy}^{3+}$  moments around  $10.68 \mu_B$ . The value of  $\chi$  at lower temperature increases in the order of  $\text{Sm227} < \text{Yb227} < \text{Gd227} < \text{Er227} < \text{Dy227}$  which can be correlated with the increase in magnetic moments of  $A^{3+}$  i.e  $\text{Sm}^{3+} < \text{Yb}^{3+} < \text{Gd}^{3+} < \text{Er}^{3+} < \text{Dy}^{3+}$ . M-T measurements of Pr227 wasn't taken, as it is reported to show no ordering up to 0.3 K [20].

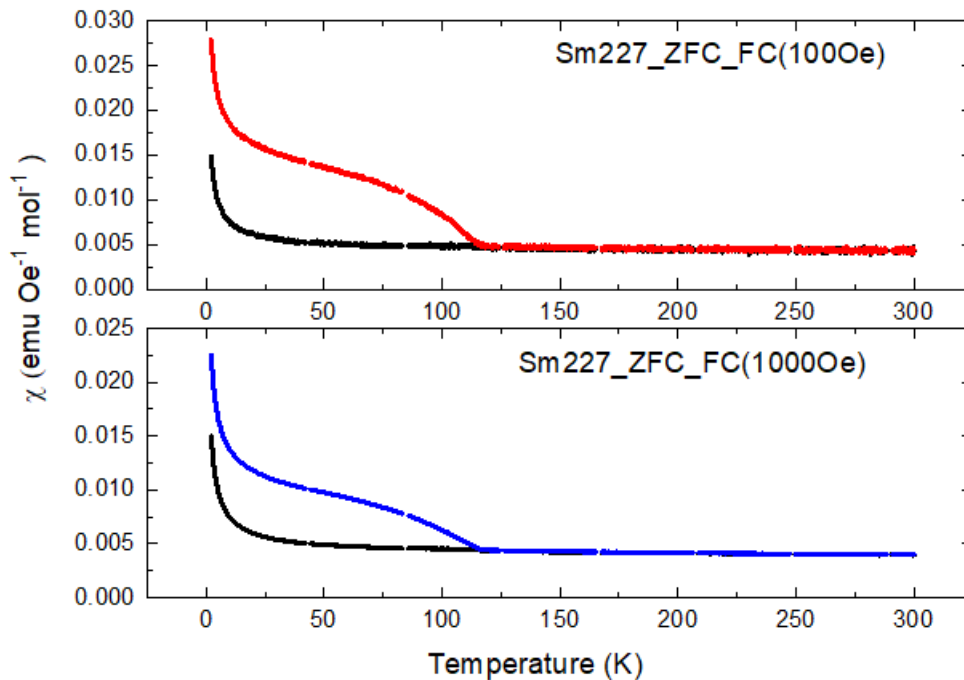
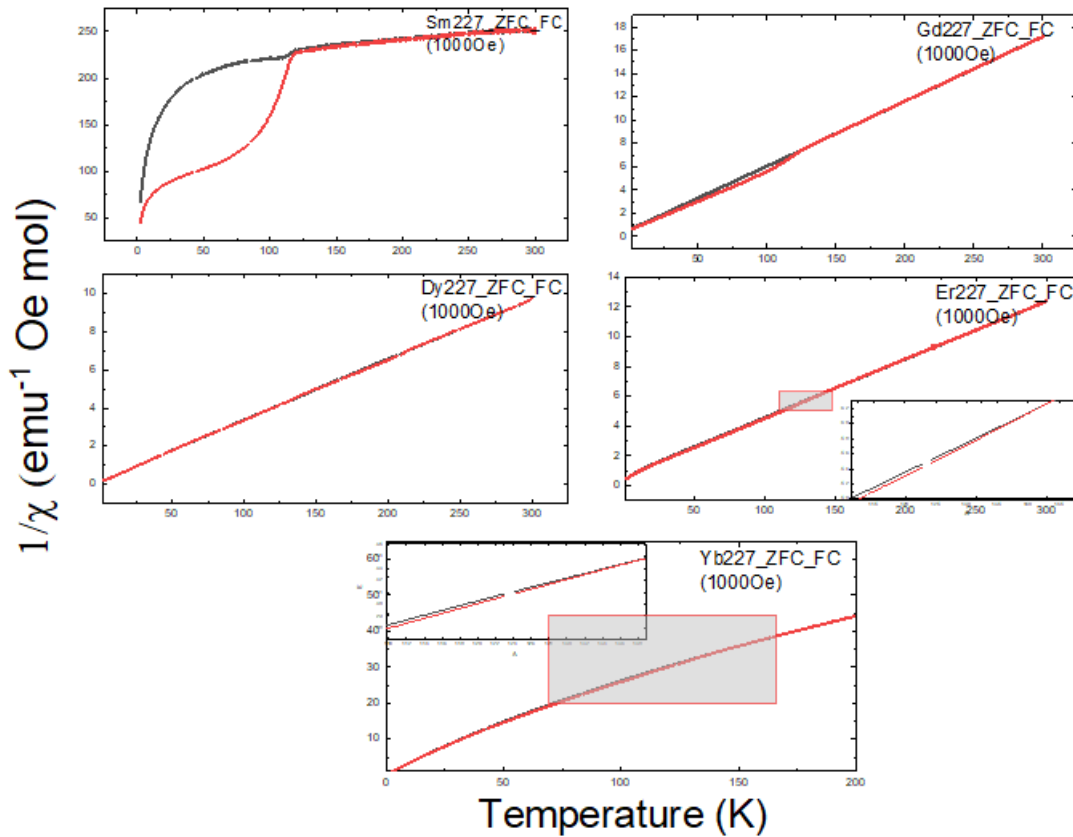


Figure 6.14:  $\chi(T)$  versus T  $A_2\text{Ir}_2\text{O}_7$ ,  $A = \text{Sm}$

Figure 6.15:  $1/\chi(T)$  versus  $T$   $A_2\text{Ir}_2\text{O}_7$ ,  $A = \text{Sm}, \text{Gd}, \text{Dy}, \text{Er}, \text{Yb}$ 

### 6.2.3 Heat capacity measurements

No sharp transitions are seen near  $T_{MI}$  for any of the samples. A representative plot of specific heat comparison with the literature for  $\text{Sm}_2\text{Ir}_2\text{O}_7$  is shown in figure 6.16. The low temperature specific heat for all the samples (1.8K to 20K) is shown in Fig 6.17. A low temperature anomaly upturn below 8K is observed for  $A_2\text{Ir}_2\text{O}_7$ ,  $A = \text{Pr}, \text{Sm}, \text{Dy}, \text{Er}$ . which can be attributed to the Schottky contribution. The occurrence of this contribution at sufficiently low temperatures give rise to a characteristic bell shaped curve skewed out on the high temperature side. In its simplest form it represents the presence of an excited level. If a two level system is considered at low temperature, it is difficult to change the total energy of the two-level system because thermal excitations cannot overcome the energy barrier. At very high temperature, the total energy of the two-level system doesn't change much with temperature, because the energy scales of thermal excitations are irrelevantly large and both levels will be nearly equally populated. When thermal excitation energy is comparable to the energy spacing, transitions from one level to another takes place and this rapid change in the internal energy corresponds to a large



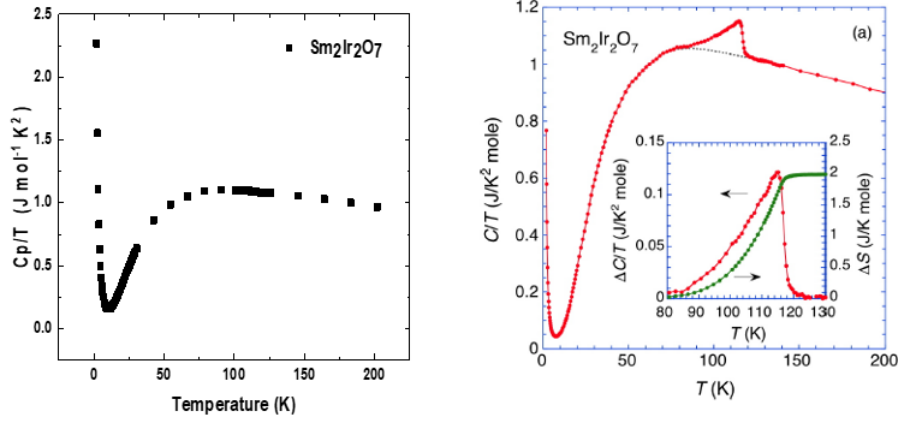


Figure 6.16: Comparison of Specific heat ( $C_p$ ) for  $Sm_2Ir_2O_7$  in the present study and literature [2]

specific heat which becomes zero at both very high and low temperatures. An upturn due to Schottky anomaly is expected in compounds containing lanthanide elements with incompletely filled f shell. Indeed there is no upturn in the specific heat  $Eu_2Ir_2O_7$  measurements of where ground state multiplicity  $J=0$  for  $Eu^{3+}$  [21]. For temperatures below 20 K, the specific heat is fitted using the formula

$$C_p = C_{sch} + \gamma T + \beta T^3,$$

$$C_{sch} = R * \left(\frac{\Delta}{T}\right)^2 * \frac{\exp\left(\frac{\Delta}{T}\right)}{\exp\left(1 + \frac{\Delta}{T}\right)^2}$$

$R$  is the gas constant,  $\Delta = \frac{\varepsilon}{k}$ ,  $\varepsilon$  is the transition energy and  $k$  is the boltzmann constant,  $n$  is 1, which is true for  $A^{3+}$  under spin orbit coupling and octahedral crystal field splitting. At low temperatures, only the long-wavelength acoustic phonons are excited. and their contribution to specific heat varies as  $T^3$ .

For  $Sm_2Ir_2O_7$  not much shift is observed in the schottky peak with the application of magnetic field where as in  $Er_2Ir_2O_7$  the peak shift to higher temperature with increasing magnetic field due to increased  $\Delta$  value as expected. In  $Sm_2Ir_2O_7$  the height of upturn is observed to be suppressed. The specific heat equation fit more accurately for  $Sm_2Ir_2O_7$ , yielding a  $\gamma$  value of  $14.56 \text{ mJ mole}^{-1}\text{K}^{-2}$ . For rest of the samples  $\gamma$  is observed to be above  $100 \text{ mJ mole}^{-1}\text{K}^{-2}$  which is too high for an insulating sample. Hence thorough analysis on how to fit low temperature specific heat with schottky anomaly has to be analysed.

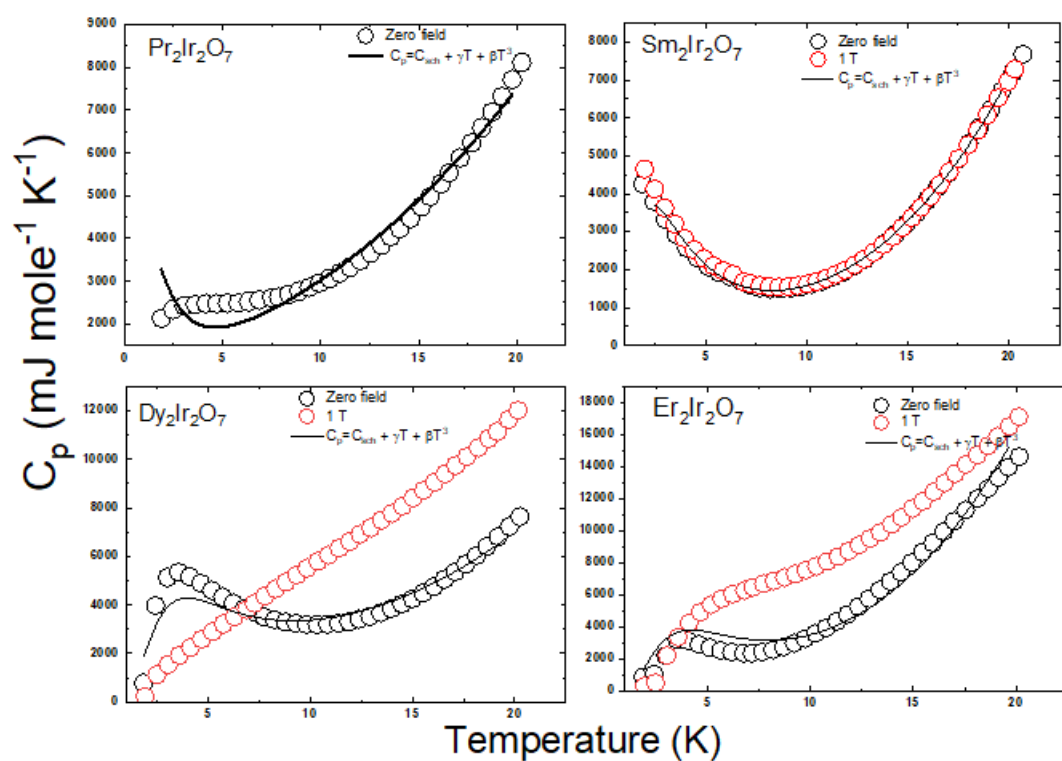


Figure 6.17: Specific heat data comparison between samples synthesized via solid state reaction and wet chemical method for  $\text{Sm}_2\text{Ir}_2\text{O}_7$

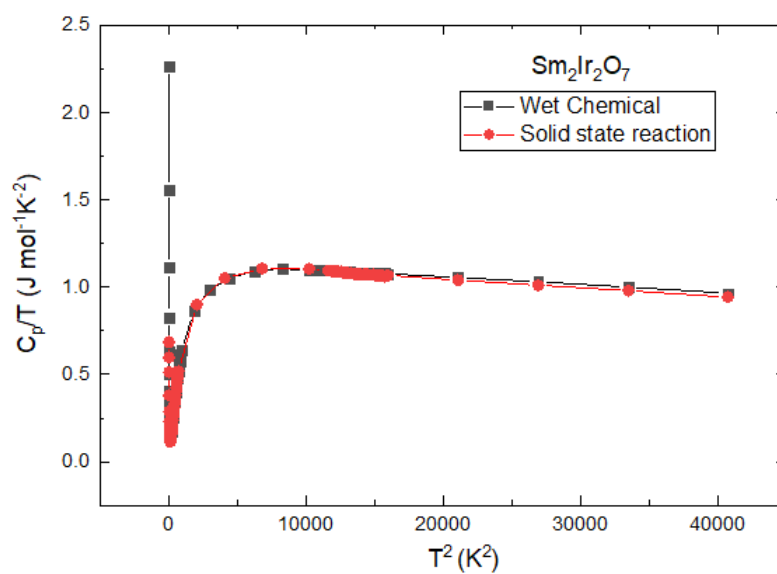


Figure 6.18: Specific heat data comparison between samples synthesized via solid state reaction and wet chemical method for  $\text{Sm}_2\text{Ir}_2\text{O}_7$

Figure 6.18 represents the comparison for specific heat data for solid state reaction route and wet chemical reaction route for  $\text{Sm}_2\text{Ir}_2\text{O}_7$ . For  $\text{Sm}_2\text{Ir}_2\text{O}_7$  the curve for both synthesis methods overlaps.

## 6.2.4 Summary and conclusions

Six samples of  $A_2\text{Ir}_2\text{O}_7$  ( $A = \text{Pr, Sm, Gd, Dy, Er, Yb}$ ) were synthesized using wet chemical method. All the synthesized sample were structurally characterized to understand the formation of Pyrochlore phase as well as the presence of impurities to understand the efficiency of wet chemical method in obtaining single phase pyrochlore iridates without multiple sintering as well as prolonged reaction time. The wet chemical is a reliable method to form single phase pyrochlore with minimum  $\text{IrO}_2$  losses.

The physical property of synthesized samples were characterized by resistivity, magnetization, and specific heat measurements. The comparison of  $\text{Sm}_2\text{Ir}_2\text{O}_7$  resistivity data for solid state and wet chemical indicates higher magnitude for former method, which was confirmed by larger number of smaller grains in its microstructure. A metal to insulator phase transition is seen in  $\text{Sm}_2\text{Ir}_2\text{O}_7$  and  $\text{Gd}_2\text{Ir}_2\text{O}_7$ . The low temperature resistivity behaviour was fitted to different equations including arrhenius plot, variable range hopping, variable range hopping with electronic correlation and WSM model. None of the samples lies in the range of WSM as the  $n$  value in  $\rho = \rho_0 T^{-n}$  is not 1, for the samples which best fits the equation. From the magnetic susceptibility data, transition to AFM ordering at  $T_N$  was confirmed and  $T_N$  is nearly same as the literature values. The low temperature specific heat for  $\text{Ln}_2\text{Ir}_2\text{O}_7$  ( $\text{Ln} = \text{Pr, Sm, Dy, Er}$ ) was measured and analysed. The data was fitted using specific heat equation which included the schottky anomaly and the electronic and phonon contributions. The equation of fit has to be analysed thoroughly to get an accurate fit so that expected  $\gamma$  values are obtained.

## 6.3 Outlook

Pyrochlore iridates are predicted to be a promising candidate for weyl semi metals. A slight variation brought in to these geometrically frustrated system, be its pressure, chemical doping can result in weyl semi metal ground state. For example recent experimental

studies of Bi doping on  $\text{Eu}_2\text{Ir}_2\text{O}_7$  reveals a weyl semi metal resistivity behaviour for 1% Bi doping in Eu site [22]. Stuffing/doping studies are lacking in pyrochlore iridates, which is an efficient method to realize different ground states. A major difficulty to this was the tricky synthesis procedure, resulting in huge  $\text{IrO}_2$ , in the conventional solid state technique. Still, single crystal of pyrochlore iridate is again a difficulty as higher temperatures are required again resulting in large precursor loss. This might be the reason for contradictory properties reported for the same sample in different literature as the final stoichiometry is different in them. The success of wet chemical synthesis route in the current research in a way is a better substitute as, there is a good control over  $\text{IrO}_2$  loss.

Recent theoretical studies on pyrochlore iridates suggest a change in the span of weyl semi metal phase realized for a range of  $U$  and  $\lambda$  value. Many of the studies consider only the interactions of itinerant 5d electrons while constructing a ground state phase diagram. When interaction of localized 4f electrons and itinerant 5d electron were considered, the weyl semi metal phase was realized for comparatively larger range of  $U$  and  $\lambda$  values. Few of the unexplained reasons for phenomena like chiral spin liquid state below 1.5 K for  $\text{Pr}_2\text{Ir}_2\text{O}_7$ , metal insulator transition at around 36 K for  $\text{Nd}_2\text{Ir}_2\text{O}_7$  could be described with new correlation term (f-d exchange) and thus obtained phase diagrams [23]. Thus more theoretical as well as experimental studies on pyrochlore iridates are necessary to unveil and realize novel ground states and their theoretical justifications.

# Bibliography

- [1] William Witczak-Krempa, Gang Chen, Yong Baek Kim, and Leon Balents. Correlated quantum phenomena in the strong spin-orbit regime. *Annu. Rev. Condens. Matter Phys.*, 5(1):57–82, 2014.
- [2] Kazuyuki Matsuhira, Makoto Wakeshima, Yukio Hinatsu, and Seishi Takagi. Metal–insulator transitions in pyrochlore oxides  $\text{Ln}_2\text{Ir}_2\text{O}_7$ . *Journal of the Physical Society of Japan*, 80(9):094701, 2011.
- [3] BJ Kim, Hosub Jin, SJ Moon, J-Y Kim, B-G Park, CS Leem, Jaejun Yu, TW Noh, C Kim, S-J Oh, et al. Novel  $j$  eff= 1/2 mott state induced by relativistic spin-orbit coupling in  $\text{Sr}_2\text{IrO}_4$ . *Physical review letters*, 101(7):076402, 2008.
- [4] Jeffrey G Rau, Eric Kin-Ho Lee, and Hae-Young Kee. Spin-orbit physics giving rise to novel phases in correlated systems: Iridates and related materials. *Annual Review of Condensed Matter Physics*, 7:195–221, 2016.
- [5] MA Subramanian, G Aravamudan, and GV Subba Rao. Oxide pyrochlores: a review. *Progress in Solid State Chemistry*, 15(2):55–143, 1983.
- [6] Daiki Yanagishima and Yoshiteru Maeno. Metal-nonmetal changeover in pyrochlore iridates. *Journal of the Physical Society of Japan*, 70(10):2880–2883, 2001.
- [7] Prachi Telang, Kshiti Mishra, AK Sood, and Surjeet Singh. Dilute doping in the pyrochlore iridate  $\text{Eu}_2\text{Ir}_2\text{O}_7$ . *Physical Review B*, 97(23):235118, 2018.
- [8] FF Tafti, JJ Ishikawa, A McCollam, S Nakatsuji, and SR Julian. Pressure-tuned insulator to metal transition in  $\text{Eu}_2\text{Ir}_2\text{O}_7$ . *Physical Review B*, 85(20):205104, 2012.
- [9] Wei Liu, Hui Han, Long Ma, Li Pi, Lei Zhang, and Yuheng Zhang. Different pressure effects in  $\text{A}_2\text{Ir}_2\text{O}_7$  ( $\text{A} = \text{Gd}, \text{Eu}, \text{and Sm}$ ). *Journal of Alloys and Compounds*, 741:182–

- 187, 2018.
- [10] Pei-Chieh Shih, Jaemin Kim, Cheng-Jun Sun, and Hong Yang. Single-phase pyrochlore  $\text{Y}_2\text{Ir}_2\text{O}_7$  electrocatalyst on the activity of oxygen evolution reaction. *ACS Applied Energy Materials*, 1(8):3992–3998, 2018.
- [11] Y Taguchi, Y Oohara, H Yoshizawa, N Nagaosa, and Y Tokura. Spin chirality, berry phase, and anomalous hall effect in a frustrated ferromagnet. *Science*, 291(5513):2573–2576, 2001.
- [12] Y Machida. Y. machida, s. nakatsuji, y. maeno, t. tayama, t. sakakibara, and s. onoda, phys. rev. lett. 98, 057203 (2007). *Phys. Rev. Lett.*, 98:057203, 2007.
- [13] M Hanawa. M. hanawa, y. muraoka, t. tayama, t. sakakibara, j. yamaura, and z. hiroi, phys. rev. lett. 87, 187001 (2001). *Phys. Rev. Lett.*, 87:187001, 2001.
- [14] S Yonezawa, Y Muraoka, Y Matsushita, and Z Hiroi. Superconductivity in a pyrochlore-related oxide  $\text{KOs}_2\text{O}_6$ . *Journal of Physics: Condensed Matter*, 16(3):L9, 2004.
- [15] Sumathi Rao. Weyl semi-metals: a short review. *arXiv preprint arXiv:1603.02821*, 2016.
- [16] Michael Hook. Topological semimetals. Master’s thesis, University of Waterloo, 2012.
- [17] C Donnerer, MC Rahn, M Moretti Sala, JG Vale, D Pincini, J Stremper, M Krisch, D Prabhakaran, AT Boothroyd, and DF McMorrow. All-in–all-out magnetic order and propagating spin waves in  $\text{Sm}_2\text{Ir}_2\text{O}_7$ . *Physical review letters*, 117(3):037201, 2016.
- [18] AM Huízar-Félix, T Hernández, S De la Parra, J Ibarra, and B Kharisov. Sol–gel based pechini method synthesis and characterization of  $\text{Sm}_{1-x}\text{Ca}_x\text{FeO}_3$  perovskite  $0.1 \leq x \leq 0.5$ . *Powder technology*, 229:290–293, 2012.
- [19] K Horigane, M Fujii, H Okabe, K Kobayashi, R Horie, H Ishii, YF Liao, Y Kubozono, A Koda, R Kadono, et al. Magnetic phase diagram of  $\text{Sr}_{2-x}\text{La}_x\text{IrO}_4$  synthesized by mechanical alloying. *Physical Review B*, 97(6):064425, 2018.

- [20] JM Ni, YY Huang, EJ Cheng, YJ Yu, BL Pan, Q Li, LM Xu, ZM Tian, and SY Li. Ultralow-temperature thermal conductivity of  $\text{Pr}_2\text{Ir}_2\text{O}_7$ : a metallic spin-liquid candidate with quantum criticality. *arXiv preprint arXiv:1807.11185*, 2018.
- [21] Edgar F Westrum Jr. Lattice and schottky contributions to the morphology of lanthanide heat capacities. 1983.
- [22] Prachi Telang, Kshiti Mishra, Giacomo Prando, AK Sood, and Surjeet Singh. Anomalous lattice contraction and emergent electronic phases in bi-doped  $\text{Eu}_{1-x}\text{Ir}_2\text{O}_7$ . *arXiv preprint arXiv:1902.03214*, 2019.
- [23] Gang Chen and Michael Hermele. Magnetic orders and topological phases from f-d exchange in pyrochlore iridates. *Physical Review B*, 86(23):235129, 2012.